THEORETICAL INVESTIGATION OF STRAIN-COMPENSATED
LASER STRUCTURES

M. Sc. Thesis

in *127728*

Engineering Physics

University of Gaziantep

By

Hüseyin TOKTAMIŞ

September 2002
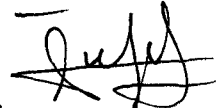
Approval of the Graduate School of Natural and Applied Sciences
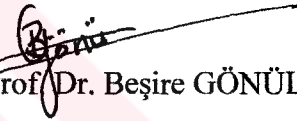
Prof. Dr. Ali Rıza TEKİN

Director

I certify that this thesis satisfies all the requirements as a thesis for the degree of Master of Science.
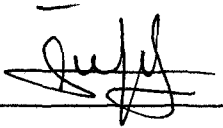
Prof. Dr. Ömer F. BAKKALOĞLU

Head of Department

This is to certify that we have read this thesis and that in our opinion it is fully adequate, in scope and quality, as a thesis for the degree of Master of Science.
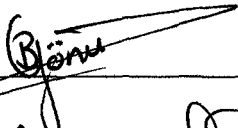
Assoc. Prof. Dr. Beşire GÖNÜL

Supervisor

Examining Committee Members

Prof. Dr. Ömer F. BAKKALOĞLU

Assoc. Prof. Dr. Beşire GÖNÜL

Assist. Prof. Dr. A. Necmettin YAZICI

ii

ABSTRACT

THEORETICAL INVESTIGATION OF STRAIN-COMPENSATED LASER STRUCTURES

TOKTAMIŞ, Hüseyin

M.Sc., Engineering Physics Department

Supervisor: Assoc. Prof. Dr. Beşire GÖNÜL

September 2002, 79 Pages

The work described in this thesis is a theoretical investigation of the effect of strain compensation optical confinement factor, conduction- and valence- band offsets, allowed energy levels, transparency and threshold carrier density, peak gain and band line-ups. Different concepts for achieving strain-compensated quantum well structures emitting around 1.3μm have been investigated. The study provides a better understanding of strain-compensated structures. The modeling of strain-compensated laser structures require a knowledge of the behavior of this novel structure in terms of gain characteristics. The work carried out in this thesis indicate that strain compensated compression active layers show better device performance compared to the strain compensated tension active layers.

Key words: strain-compensated structures, compression, tension, optical confinement factor, optical gain.

ÖZ

ZORLANMA TELAFİLİ LAZER YAPILARININ TEORİK OLARAK İNCELENMESİ

TOKTAMIŞ, Hüseyin

Yüksek Lisans Tezi

Fizik Müh. Bölümü

Tez Yöneticisi: Doç. Dr. Beşire GÖNÜL

Eylül 2002, 79 sayfa

Örgü sabitleri farklı olan tabakalar birbiri üzerine büyütüldüğünde orijinal örgü sabitinde germe ve sıkıştırma olmak üzere iki tür değişiklik oluşur ve buna orijinal uzunluğuna nazaran oluşan değişim (strain) denir. Kuyudaki değişim engele uygulanan değişim ile nötürleştirebilir. Bu tür yapılar malzemenin bant yapısında çok büyük değişiklikler oluşmasına sebep olur. Bu tezde bu tür yapıların optiksel hapsolma faktörü, iletim ve yalıtım bandı derinliği, izinli enerji seviyeleri, geçirgenlik ve eşik taşıyıcı yoğunluğu ve kazanç üzerindeki etkileri teorik olarak incelendi. Farklı yapılar ile karşılaştırılıp bu yapıların daha iyi anlaşılabilmesini sağlayabilecek hesaplamalar yapıldı.

Anahtar kelimeler: Optiksel hapsolma faktörü, iletim ve yalıtım bandı derinliği, eşik taşıyıcı yoğunluğu.

ACKNOWLEDGEMENT

TABLE OF CONTENTS

CHAPTER 1

INTRODUCTION

The synthesis of semiconductor heterostructures is gaining greater importance due to the demands of modern electronic devices. Both the need for novel electronic properties and the use of low cost substrates have led to the consideration of lattice-mismatched materials based heterostructures. One important issue facing heteroepitaxy is related to the lattice-mismatch induced strain that limits the accessible layer thickness before the observation of structural defects necessary to relieve the stress. While the thickness limit (critical thickness, h_c) can reach few thousand Angstroms for mismatch values not exceeding a fraction of a percent, the value of h_c is greatly reduced (to few Angstroms) when the mismatch value reaches 3–6%. From an electronic standpoint, a lattice mismatch in excess of 2% yields notice-able band gap modifications making this type of systems interesting. However, the usefulness of such thin induced energy bands displacement is very limited. A way of achieving thick layers subjected to high-strain values is to use the principle of strain compensation. Strain-compensation techniques prevent the formation of dislocations by alternating layers with compressive and tensile-strain of equal amounts resulting in zero-net strain. This technique may be used to increase the number of compressively strained wells without inducing defects.

In recent years, considerable attention and much effort have been focused on the development of strain-compensated multiple quantum well (SCMQW) material and devices, such as diode lasers and electroabsorption modulators, owing to their excellent features and wide applications in optical communication systems, particularly in optical

1

signal and data processing. Strain-compensation technique must be taken into account in optoelectronic device engineering and has been shown as an attractive technique for fabrication of photonic integrated circuits

InGaAsP-based multiple quantum well structures with alternating compressive- and tensile-strained layers are promising for optoelectronic device applications. InGaAsP/InP quantum well (QW) structures have been widely used in fabricating communication lasers operating at 1.3μm and 1.55μm wavelengths. While the early work was centered on unstrained QW structures, interest has shifted to strained QW's because of several advantages that the latter provides. These advantages include enhanced gain, increased differential gain, low threshold current density, increased modulation bandwidth, and reduced line width enhancement factor. Both tensile strained and compressively strained QW's have been studied, and the choice of a particular QW design is very much dictated by the application of the device. For example, lasers to be used in loop applications are required to have superior performance over a wide range of temperatures such as 40°C to 90°C. These lasers should maintain high differential quantum efficiency even at 90°C in an uncooled environment, and it has been shown that this performance is achieved by increasing the number of QW's. However, in the case of strained QW structures, increasing the number of QW's may lead to strain relaxation, thereby generating misfit dislocations. This consideration has led to the use of zero net strained QW's containing wells and barriers with alternating strain to increase the total QW thickness. A few reports have appeared in the literature discussing the growth of strain-compensated InGaAsP/InP QW's for 1.5 μm lasers.

The following sections give a brief overview of the work described in this thesis.

Chapter 2 summarizes the benefits of strain-compensated structures. A review of the investigations on strain-compensated structures have been provided and the effects of the strain compensated structures on the linewidth enhancement factor, gain, differential gain and threshold current density have been mentioned.

In the first part of chapter 3, a brief description of strain theory is presented. Some analytical expressions are also presented to calculate the material parameters such as effective masses, band gap lattice constant, etc. The concept of the strain compensation is briefly introduced and the compensation alloy fraction values are

2

calculated for two types of strain compensated structures. In the second part of the chapter 3, a model calculation of optical confinement factor Γ is introduced for multiple quantum wells. It is shown that the compensation of tensile active layers with compressively strained barriers result higher optical confinement values. The effect of strain compensation on optical confinement factor is one of the important factor which determines the performance of quantum well lasers. We believe strain compensated laser structures will increase the performance of lasers.

The relative alignments of the band edges of the well and barrier material play a significant role while modeling the band structure. Therefore, in chapter 4, we present a comprehensive theoretical model for the calculation of the band edge profile of strain compensated tensile and compression active layers. The number of the confined levels and the distance between them also play a significant role during modeling the band structure. So an investigation of this issue is also the subject of chapter 4.

An idealized parabolic band model is introduced in chapter 5. The material gain characteristics are calculated by means of this idealized band model. The comparison of the strain compensated laser structures with their uncompensated correspondings are also presented.

A strain compensated structure is an ideal candidate to separate the heavy- and light- hole states spatially, i.e. to confine them into different layers producing Type-II line-up. In chapter 6, we first mention the advantages of having such alignment. Then, we determine the type of the band alignments in our strain-compensated structures.

Finally, we draw some conclusions regarding the potential advantage of strain compensated structures on the band properties in chapter 7.

CHAPTER 2

LITERATURE SURVEY

2.1 Introduction

Over the last years, strained-layer multiple quantum well (MQW) structures with lattice-matched barriers have been widely developed for optoelectronic devices. In this structure, there is a compressively or tensiley strain in the well (or active layer) and there is no strain in barriers. As the number of strained quantum wells is increased, the total strain in the structure accumulates and the total strained-layer thickness approaches a critical thickness at which lattice misfit dislocation start to form [1]. For some laser configurations, for example: short-cavity lasers, a large number of quantum wells may be required for optimal performance [2]. It is well known that incorporating strain in multiple quantum-well (MQW) laser active regions results in significant improvements in laser performance [3]. However, the incorporation of strain limits the number of quantum wells (QW's) that may be used without inducing an unacceptably high density of misfit dislocations.

Strain-compensation techniques prevent the formation of dislocations by alternating layers with compressive and tensile-strain of equal amounts resulting in zero-net strain. This technique may be used to increase the number of compressively strained wells without inducing defects. With using strain-compensated structure, higher gain, higher differential gain, lower threshold current and lower linewidth enhancement factor (α) have been obtained when strain-compensated structure has been compared with conventional strain quantum well laser.

A new type of modulator which has a strain-compensated structure with a combination of compressive wells and tensile barriers has been developed. This

4

strain-compensated structure is superior in frequency response to the conventional non-strained quantum wells because the strain-compensated structure forms shallow wells in the valance band, which reduces the hole escape time from the wells. Therefore higher speed operation can be achieved with this structure. The strain-compensated structure also provides deep wells in the conduction band. This increases the absorption coefficient and makes the modulator operate at a lower voltage. The presence of strain-compensated structure in the modulator improves its performance.

Strain-compensated quantum well lasers are being developed in the hopes of improved performance: lower threshold current, higher modulation bandwidth and lower frequency chipping. However, few experimental reports [4] exist to allow for reliable extraction of key parameters, such as gain, differential gain, and linewidth enhancement factor, thus, hindering the device design and optimization. It is, thus, more important than ever to be able to calculate these important material parameters from first principles. The first calculation of these parameters based on density matrix method and the model solid theory [5-6] which are presented by Tan et.al.[7]. The two major obstacles for such calculation are the determination of the strain-dependent band-offsets at the interface of ternary and quaternary materials and the extraction of the strain dependent anisotropic masses. These obstacles are overcome by incorporating the model solid theory [6,8] and the approximate $k.p$ method [9] into Tan's et.al. model. The density matrix [10] is then used to calculate the complex susceptibility of the Strain compensated quantum well directly, hence the gain, index change, and linewidth enhancement factor can be computed simultaneously avoiding the numerical difficulties associated with performing Kromers-Kronig transformation over limited range. Also many-body effects are considered by incorporating bandgap renormalization [11,12].

The following section summarizes the most favorite strain-compensated structures.

2.2 Strain Compensated InGaAs-GaAsP-InGaP Active Regions for $1\,\mu$m Wavelength Lasers

Dutta *et. al.* [4] reported the performance characteristic of InGaAs-GaAsP-InGaP strain-compensated laser emitting near 1μm. Their strain-compensated

structure is shown in Fig.2.1. They have studied four 60-Å–thick undoped $In_{0.2}Ga_{0.8}As$ QW active layers surrounded by 125-Å-thick $GaAs_{0.8}P_{0.2}$ barrier layers. For this composition, the lattice constant of $In_{0.2}Ga_{0.8}As$ is about 1.5% larger than that for GaAs. This results in compressively strained active region for the InGaAs-GaAs laser emitting 1 μm. The lattice constant of $GaAs_{0.8}P_{0.2}$ is about 0.8% smaller than that of GaAs. The active layer structure is sandwiched between P-InGaP and N-InGaP cladding layers. The InGaP layers are lattice matched to GaAs. The epitaxial structure has been grown by metal organic chemical vapor deposition (MOCVD) growth technique.
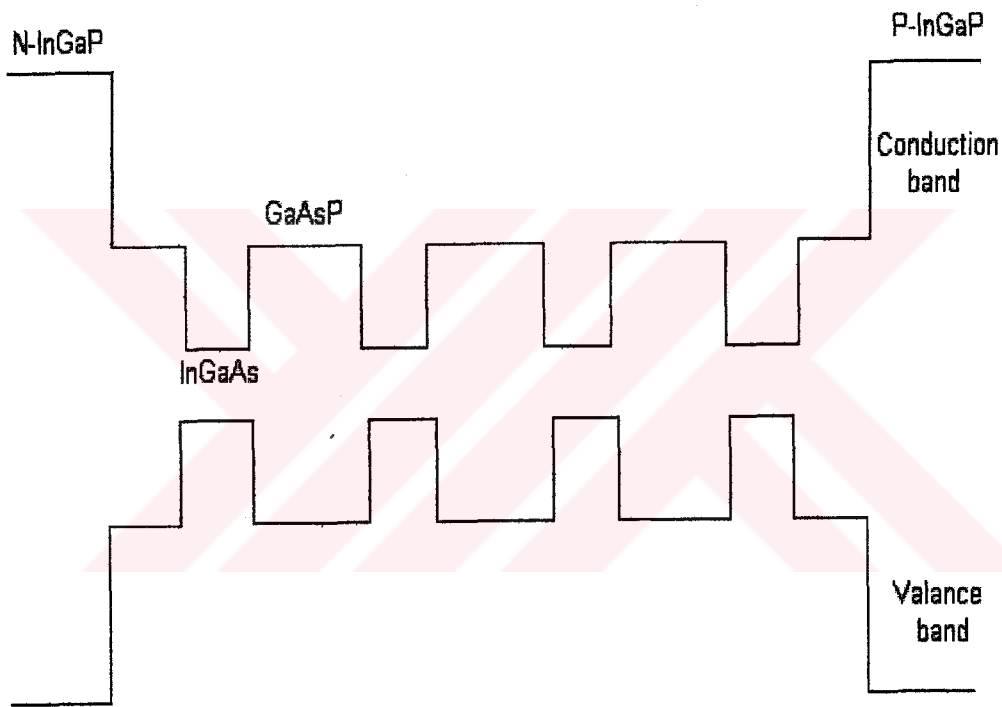
Fig.2.1 Schematic of strain compensated laser design.

The measured linewidth enhancement factor (α) is shown as a function energy in Fig.2.2. The laser photon energy is denoted by the arrow. The value of α at the lasing wavelength is 0.4 ± 0.1 . For comparison the value for a regular strained $In_{0.2}Ga_{0.8}As$-GaAs laser is 1.0 [13]
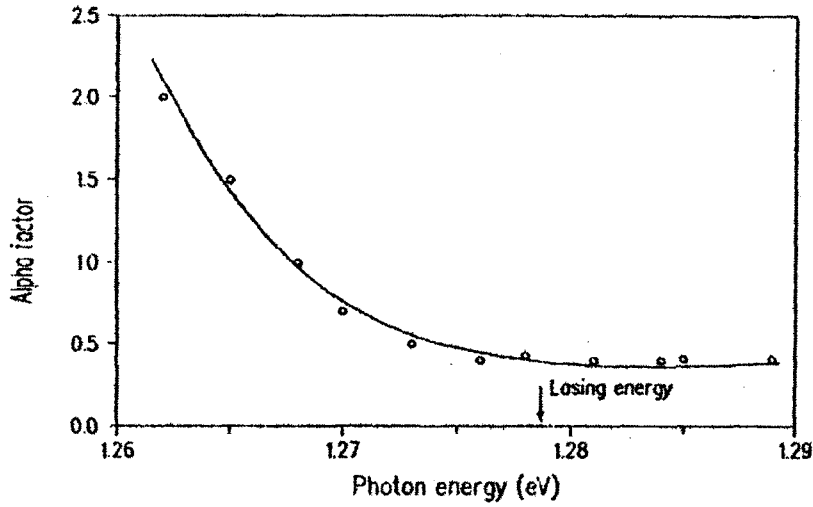
Fig.2.2 Linewidth enhancement factor (α) versus photon energy. Taken from [13].

G. L. Tan and J. M. Xu [7] have studied on this subject with the same model of N. K. Dutta and his friends. They compared strain-compensated $In_{0.2}Ga_{0.8}As$-$GaAs_{0.8}P_{0.2}$ system with a conventionally strained $In_{0.2}Ga_{0.8}As$-GaAs and observed higher gain, higher differential gain and small linewidth enhancement factor than conventionally strained QW's. This comparison has given in Table 2.1.

Table 2.1 Band offset parameters for strain compensated and uncompensated structures

	$In_{0.2}Ga_{0.8}As$	$GaAs_{0.8}P_{0.2}$		$In_{0.2}Ga_{0.8}As$	$GaAs$
a_0	5.734	5.612	a_0	5.734	5.653
E_g^{hh}	1.253491	1.612871	E_g^{hh}	1.218239	1.421
E_g^{lh}	1.360347	1.564079	E_g^{lh}	1.297362	1.421
ΔE_c	0.144600		ΔE_c	0.147655	
ΔE_v^{hh}	0.21478		ΔE_v^{hh}	0.104792	
ΔE_v^{lh}	0.05912		ΔE_v^{lh}	0.010757	
m_c	0.06220	0.08600	m_c	0.06220	0.0700
m_{hh}^{z}	0.079742	0.099679	m_{hh}^{z}	0.123822	0.35000
m_{hh}^{t}	0.342879	0.171337	m_{hh}^{t}	0.588468	0.35000
m_{lh}^{z}	0.161511	0.407872	m_{lh}^{z}	0.093845	0.07300
m_{lh}^{t}	0.063229	0.150431	m_{lh}^{t}	0.058711	0.07300

Table 2.1 shows the calculated band offsets for both structures. The superscript xy denotes parallel to the heterointerface and z denotes perpendicular to the heterointerface. They observed that the band gap difference between the tensile barrier and the compressively strained QW is greater than the conventionally strained QW structure leading to a factor of 2 increase in the HH (heavy hole) band offset. More specifically, the HH band shifts above the LH (light hole) band in the compressively strained QW layer while the reverse occurs in the tensile barrier thus also contributing to the increase in the HH band offset. Moreover, the effective mass along the heterointerface with the tensile barrier has a much smaller value than in the purely compressively strained QW.

Fig.2.3 shows the comparisons of gain spectra for the strain-compensated (SC) and the conventionally strained QW lasers for carrier concentrations of 2, 3, and $4x10^{18}$ cm^{-3}. Fig.2.4 gives a comparison of the peak gain and differential gain of the strain-compensated and conventionally strained QW lasers. They observed that the SC structure's maximum gain is almost double that of the strained structure and with its differential gain increased by 60%. The calculated peak gain wavelength is consistent with the experimental lasing wavelength of 0.97 μm [4].
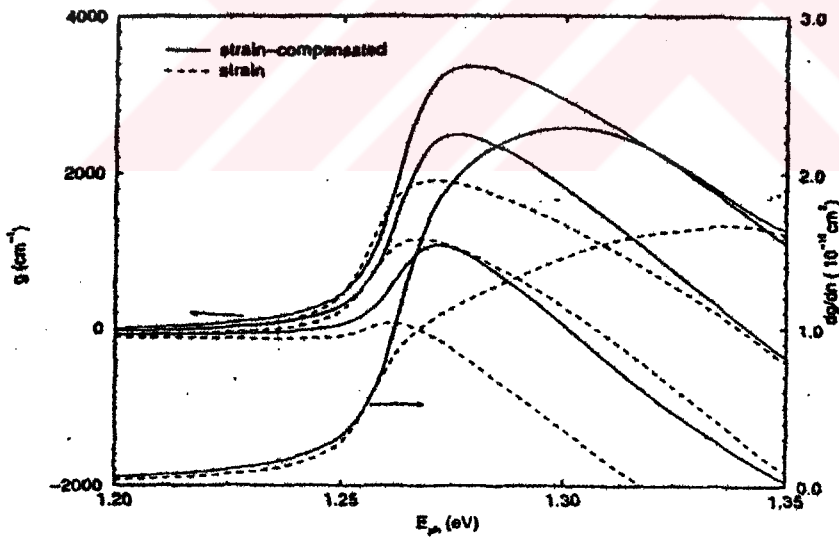
Fig.2.3   Comparison of gain and differential gain spectra for a strain compensated and a conventionally strained QW laser

8
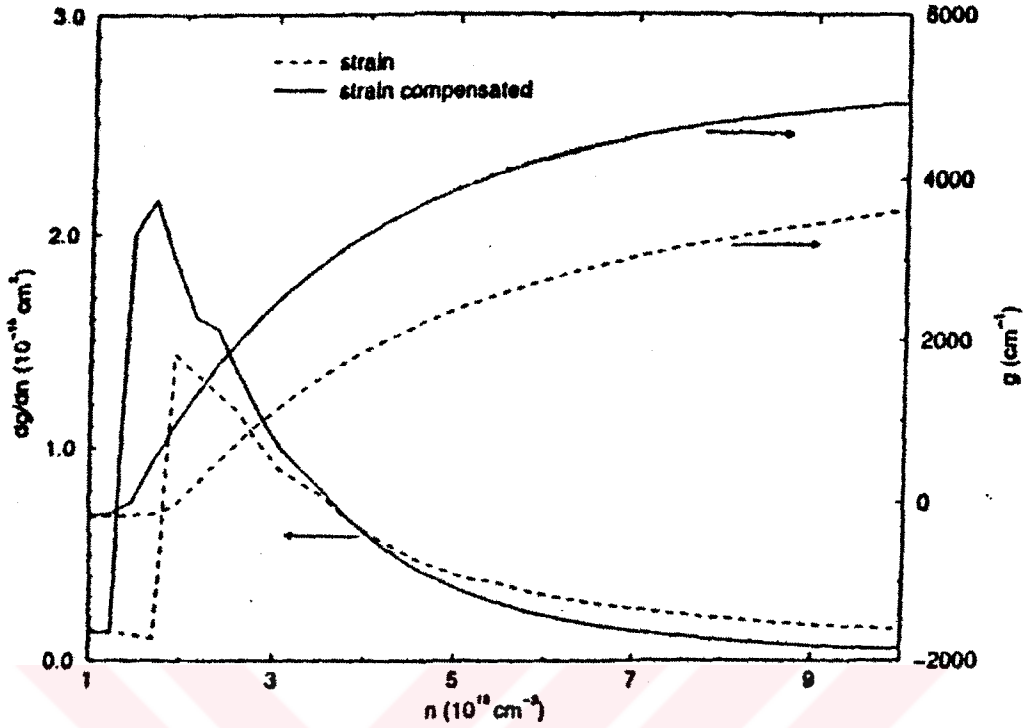
Fig.2.4 Maximum gain and differential gain versus carrier concentration. Order of dg/dn is 10^{-15} cm^2, g is 10^{-15} cm^{-1}, and n is 10^{18} cm^{-3}.

It can be seen from Fig.2.4 that due to the high gain of the SC structure, its carrier concentrations are far smaller than for the conventionally strained structure in the typical range of 2000-4000 cm^{-1} (corresponding to the modal gain range of 20-40 cm^{-1}). This results in a lower current and current density to produce the same optical power. The SC structure has a higher differential gain of 2.05×10^{-15} which is similar to the experimental estimated value of 2.1×10^{-15} [4]. Because the relaxation oscillation frequency of a laser is proportional to the square root of the differential gain at a given optical power, the SC structure offers a higher relaxation oscillation frequency and bandwidth.

The linewidth enhancement factor (α) is a key parameter that determines the spectral width of a laser under both CW (continuous wave) operation and high-frequency modulation [14].

9
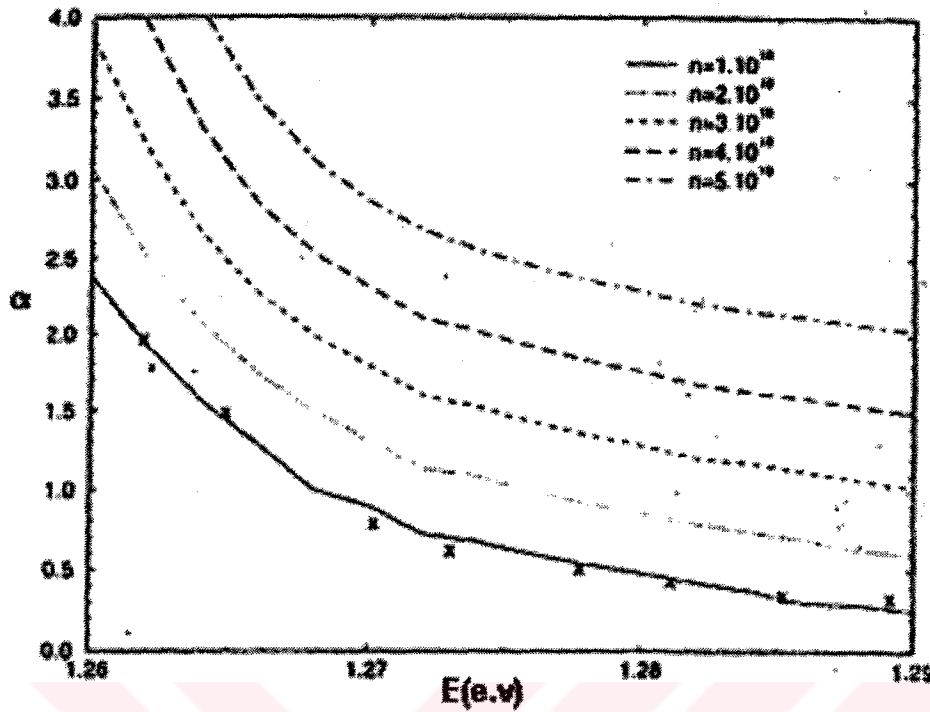
Fig 2.5 The linewidth enhancement factor (α) for SC structure as a function
of energy.

It characterizes the spectral width broadening due to fluctuations in the carrier
density that changes both the real and imaginary part of the index. The factor (α) is
the ratio of the change of the refractive index (n) with carrier density (N) to change in
optical gain (g) with carrier density. This is expressed as [14]

$$\alpha = \frac{4\pi}{\lambda} \frac{dn/dN}{dg/dN} \qquad (2.1)$$

where λ is the wavelength of the light. Fig 2.5 shows the linewidth enhancement
factor (α) for SC structure as a function of energy. It is seen from Fig.2.5 that α
increases with increasing carrier concentrations. From calculations , the SC structure
has a slightly large index change, but due to its greater differential gain, it still has a
lower α factor in a typical modal gain range.

2.3 Strain-Compensated InGaAs-InGaAsP-GaAs Active Regions Emitting for 0.98 μm Wavelength Lasers

Seoung *et. al.* [15] have studied strain compensated InGaAs/InGaAsP quantum well lasers lattice matched to GaAs with 8 nm well width and 10 nm barrier width at 300K. According to their experiment, when there is no strain in barrier (in other words , the system is uncompensated), threshold current density J_{th} is 100 A/cm^2. When the tensile strain is applied, J_{th} decreases exponentially. This reduction is explained due to the reduced transparency carrier density and the increased differential gain at transparency. This comparison has been given in Table 2.2.

Table 2.2   The variation of threshold current density as a function of barrier strain

Barrier tensile strain(%)	J_{th}(A/cm^2)
0.0	100
0.2	98
0.4	96
0.6	94
0.8	92.5
1.0	91.0

For the laser structure with tensile barriers and compressive wells, the potential well depth related to the valance band (hh) in the active layer is increased, while that related to the conduction band is decreased. However, because barriers with tensile strain have a larger bandgap than barriers lattice matched to GaAs, the potential well depth related to both the conduction and valence band is increased. For example, for zero-net strain InGaAs/InGaAsP and uncompensated InGaAs/InGaAsP lasers, well depths are 206 and 146 meV in the valence band and 303 and 246 meV in the conduction band, respectively.

2.4 Strain-Compensated InGa(As)P-InAsP Active Regions for 1.3 μm Wavelength Lasers

Tensile-strained InGaP barriers and compressively-strained InAsP QW's are one means for achieving strain-compensation (see Fig.2.6a). Interest in InGaP barrier lasers has increased due to the potential for higher T_0 values as well as higher gain owing to the large bandgap difference of 550 meV between the InGaP and 1.3 μm wavelength QW's [2], [14]. As J. C. Dries et. al. has shown in their study, the large bandgap difference between the waveguide region and the InGaP barriers reduces the internal quantum efficiency, thus increasing the threshold current density. Reducing the QW barrier bandgap using tensile-strained InGaAsP instead of InGaP (see in Fig.2.6b) increases carrier capture in the QW's, resulting in higher quantum efficiency lasers. Utilizing narrow bandgap tensile-strained InGaAsP instead of wide bandgap InGaP barriers in strain-compensated lasers, they have observed a reduction in threshold current density from 675 to 310 A/cm^2 and in T_0 from 75 K for 65 K for 2 mm long seven quantum well devices.
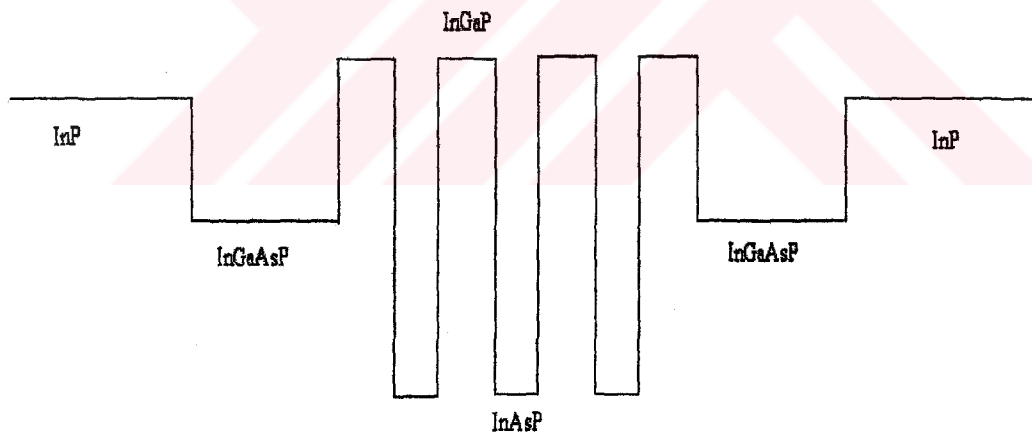
(a)
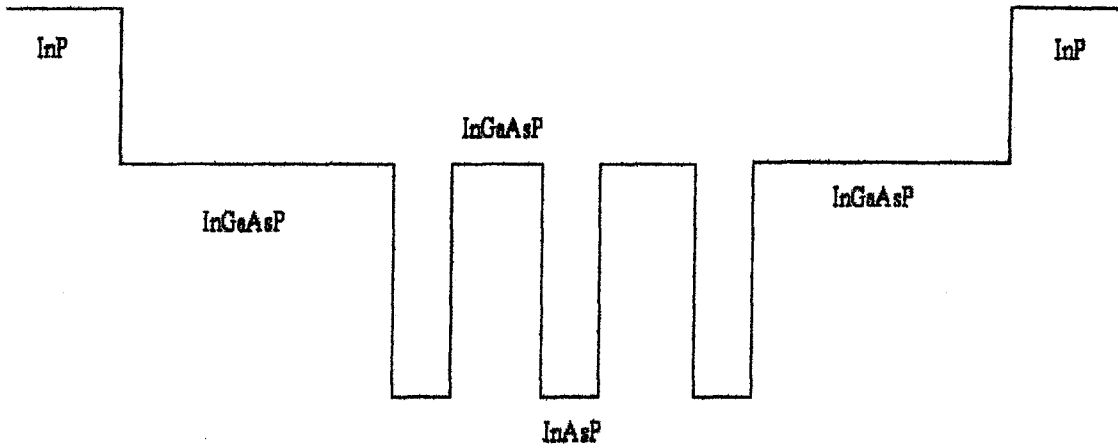
(b)

Fig.2.6 Schematic diagram of (a) InAsP-InGaP-InP strain-compensated structure
and (b) InAsP-InGaAsP-InP strain-compensated structure

Table 2.3   Quantum well and barrier widths, confinement factor per well (Γ_w),
internal losses (α_i), efficiencies (η_i) and threshold current (J_0), Gain (G_0) for the
various laser structures. The data is taken from [16].

Material	Barrier Width(Å)	QW Width(Å)	Γ_w(%)	α_i	η_i	J_0	G_0
7QW TQSC	164	62	1.18	9.1	67%	63	675
3QW TQSC	164	62	1.24	7.3	73%	88	798
SQW TQSC	164	62	1.4	2.6	52%	92	864
7QW SC	80	70	1.25	5.3	40%	80	540
3QW SC	80	70	1.33	9	54%	85	745
7QW CS	120	70	1.25	7.8	40%	NA	NA
3QW CS	120	70	1.28	10	82%	85	610

Table 2.3 summarizes and compares all the gain related parameters for the mentioned
laser structures.

13

2.5 Summary

This chapter summarizes the benefits of strain-compensated structures . Strain modifies the band structure of the quantum well structures and improves the performance of optoelectronic compared to devices with lattice-matched quantum structures. However, the total thickness of the strained material that can be grown without defect generation in these materials is limited to about 20 nm for typically 1% strain. By strain compensating with opposite strain in the barrier, it is possible to increase the number of quantum wells above the conventional limits. Strain compensation also gives access to a wider range of material compositions, and thus improved possibilities to select band-edge offsets tailored to specific device needs. Therefore, growth parameters can be optimized by means of strain compensation which allows large number of wells to be grown.

CHAPTER 3

STRAIN COMPENSATION AND ITS EFFECT ON OPTICAL CONFINEMENT FACTOR

3.1 Introduction

Strain compensation gives access to a wider range of material compositions, and thus improved possibilities to select band-edge parameters tailored to specific device needs.

The aim of this chapter is to optimize the growth parameters so that strain compensation is achieved, allowing large number of wells to be grown, and to compare the usefulness of different structures for optoelectronic devices.

3.2 Strain Theory

Semiconductor heterostructures can be grown epitaxially with two materials that are not perfectly lattice-match, provided this mismatched is not to large. Fig.3.1 shows a schematic representation of the growth of (a) a compressively strained layer in which the bulk lattice constant of the overlayer is larger than that of the substrate, and (b) the tensile strained layer in which the lattice constant of the overlayer is smaller than that of substrate. The overlayer must match the in-plane lattice constants of the substrate. Too large a mismatch may prevent epitaxiall growth altogether or lead to fractures and undesirable effects. The semiconductor epilayer is biaxially

15

strained in the plane of substrate, by an amount $\varepsilon_{\parallel}$, and uniaxially strained in the perpendicular direction, by an amount $\varepsilon_{\perp}$.
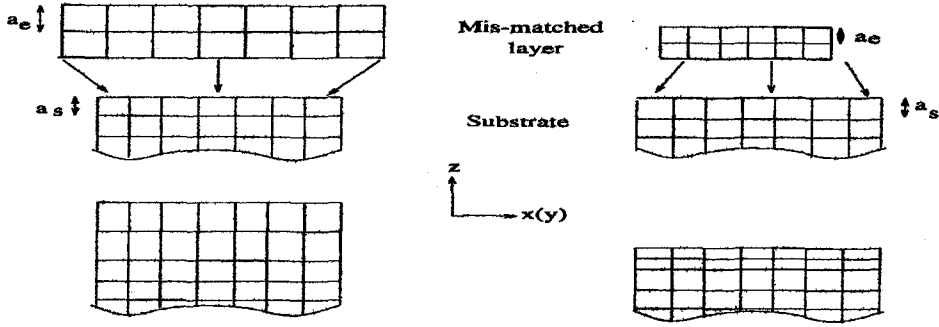
Fig.3.1   A schematic representation of (a) a compressively strained layer (b) a tensiley strained layer.

For a thick substrate, the in plane strain of the epilayer is determined from the bulk lattice constants of the substrate material, a_s, and the layer material, a_e;

$$\varepsilon_{\parallel} = \frac{a_s}{a_e} - 1$$

(3.1)

For $a_e > a_s$, i.e. $\varepsilon_{\parallel} < 0$, the epitaxial layer is under biaxial compressive strain, while for $a_e < a_s$, the strain is tensile. For compound materials, the epilayer lattice constant a_e can be calculated from interpolation method.

3.3   Material Parameters

3.3.1   Band edge effective mass

Effective mass is one of the important parameter which determines the behavior of the quantum system. The valence band effective mass can be written in terms of Luttinger's parameters of γ_1 and γ_2 as [17]

$$m^*_{hh,lh} = \frac{m_0}{\gamma_1 \pm 2\gamma_2}$$

(3.2)

Equation (3.2) shows the perpendicular effective mass for valence band. Positive sign corresponds to the mass of the light-hole(LH) and negative sign corresponds to

16

the mass of the heavy hole (HH). Similarly, in-plane effective mass can be expressed as

$$m^*_{hh,lh} = \frac{m_0}{\gamma_1 \mp \gamma_2} \qquad (3.3)$$

The corresponding effective mass values for quarternary and ternary material can be calculated from interpolation method (in terms of binaries). Table 3.1 summarizes the band structure parameters for binary materials used in the interpolation method.

Table.3.1 The band structure parameters for GaAs, InAs, InP, GaP [18].

Parameters	GaAs	InAs	GaP	InP
γ_1	6.98	20	4.05	5.08
γ_2	2.06	8.5	0.49	1.6
A_0(Å)	5.6533	6.0584	5.4512	5.8688
m^*	0.067	0.023	0.17	0.08

The conduction band effective mass for $In_{1-x}Ga_xAs_yP_{1-y}$ can be found from the following Equation of [19] ;

$$m_c = 0.08 - 0.116x + 0.026y - 0.059xy + (0.064 - 0.02x)y^2 + (0.06 - 0.032y)x^2 \qquad (3.4)$$

The conduction band effective mass for $In_{1-x}Ga_xP$ is calculated from interpolation method.

3.3.2 Interpolation method

To obtain most parameters for ternary and quarternary material systems, a linear interpolation between the parameters of the relevant binary semiconductor is used. The interpolation formulas for all physical parameters P used in the calculation are given for quarternary material as

$$P(A_{1-x}B_xC_yD_{1-y}) = P(BC)xy + P(BD)x(1-y) + P(AC)(1-x)y + P(AD)(1-x)(1-y), \qquad (3.5)$$

and for ternary material

17

$$P(A_{1-x}B_xC) = P(AC)(1-x) + P(BC)x \qquad (3.6)$$

3.4 Strain Compensation Technique

It is well known that incorporating strain in multiple quantum-well (MQW) laser active regions results in significant improvements in laser performance [3]. However, the incorporation of strain limits the number of quantum wells that may be used without inducing an unacceptable high density of misfit dislocations. Strain-compensation techniques prevent the formation of dislocations by alternating layers with compressive and tensile-strain of equal amounts, resulting in zero-net strain. It is possible to have closely strain-compensated or partially strain-compensated active region by means of the following balance equation of

$$N_w t_w \varepsilon_w + N_b t_b \varepsilon_b \cong 0 \qquad (3.7)$$

where N_w and N_b are the number of wells and barriers, t_w and t_b are the thickness of well and barrier, ε_w and ε_b are the lattice constant differences between the active region and substrate and barrier region and substrate.

Since ε_w and ε_b are of opposite sign, it is possible to satisfy Eqn.(3.7) by choosing proper t_w and t_b for given values of ε_w and ε_b. The light emitting layers in the strain-compensated multiquantum-well (MQW) laser are effectively under a larger amount of compressive stress than that for a regular strained MQW laser. This effect results in larger gain coefficient and smaller linewidth enhancement factor for strained compensated laser relative to conventional strained layer lasers.

3.5 Strain Compensated Structures

The most favorite strain compensated laser structures are summarized in Chapter 2. In those studies, authors compared their strain-compensated laser in which well is under compression with a conventionally strained laser and found that strain compensated laser has a higher gain and differential gain. In this thesis, we compare two types of strain compensated systems with each other. To evaluate this we use the following strain-compensated structure of

18

i) QT(cs) structure: Well is under compressive strain and barrier is under tensile strain,

ii) QT(ts) structure: Well is under tensile strain and barrier is under compression strain.

3.5.1 QT (cs) structure

This type of strain-compensated quantum well structure denotes compressive $In_{1-x}Ga_xAs_yP_{1-y}$ wells with a constant Ga fraction which is held at 0.11 and tensile barriers. This Ga fraction is the best for this structure to obtain compression in the well and tension in the barrier for the range of wavelengths which varies from 1.27μm to 1.55μm. The use of $In_{1-x}Ga_xP$ barriers in this structure causes the advantage of very deep electron wells, which may be essential for achieving good high temperature laser performance. The wellwidth and barrier width are fixed at 50Å and 94Å. The number of wells is equal to the number of barriers. Arsenide fraction of the well changes from 0.54 to 0.74 to obtain lasing wavelength which varies from 1.27μm to 1.55μm.
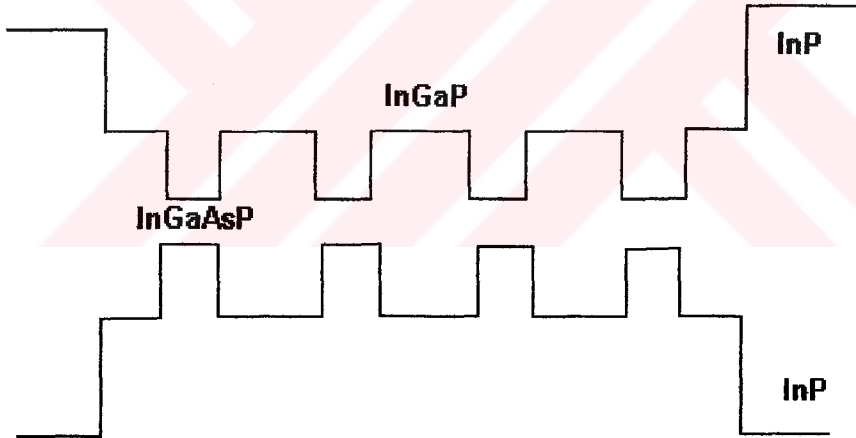

Fig.3.2 The schematic diagram for QT (cs) structure. QT stands for quarternary and cs stands for compressively strained active layers.

Barrier content depends on well content by the following relation of

$$x_b = \frac{(a_s - 5.4512 - \varepsilon_b * 5.4512)}{0.4176 * (\varepsilon_b + 1)} \qquad (3.8)$$

where a_s is the lattice constant of substrate (InP) and ε_b is the barrier strain. This relationship can be obtained from equation (3.7) and proof is given in Appendix A.
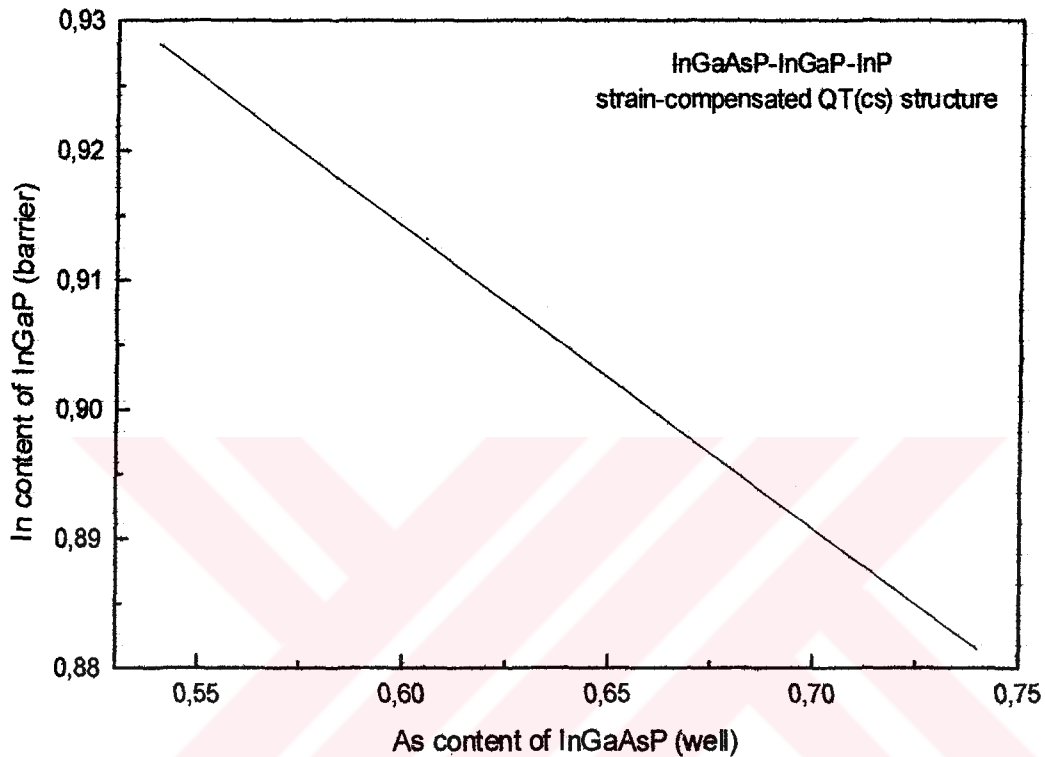
Fig.3.3 Indium content of InGaP (barrier) versus arsenide content of InGaAsP (well) to obtain strain-compensated QT(cs) structure.

Fig.3.3 shows the In content of InGaP (barrier) as a function of As content of InGaAsP (well) for the strain-compensated QT (cs) structure . This figure has been plotted according to the equation (3.8). In this region, well is always under compression and barrier is under tension. The range of the strain of the well changes from −0.96% to −1.599 % and strain of the barrier changes from 0.513% to 0.85%, when the As content of the well changes from 0.54 to 0.74.
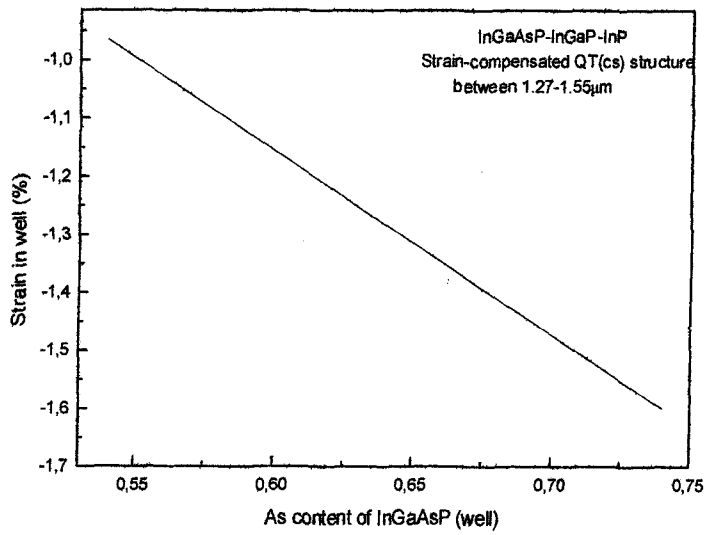
(a)
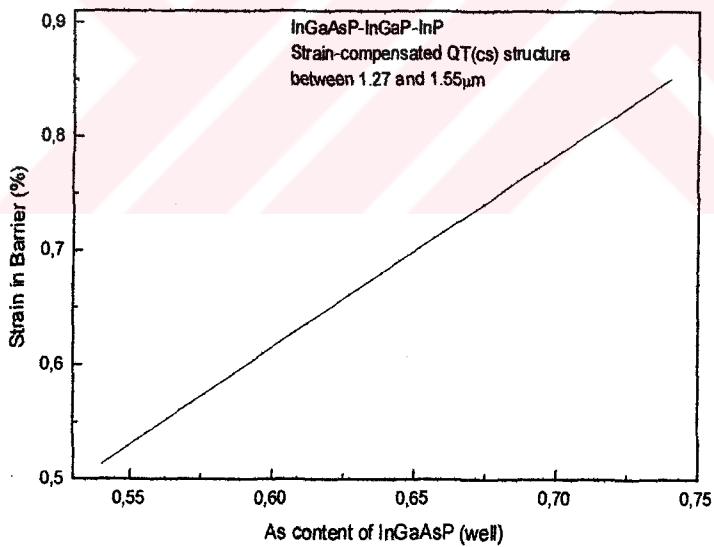
(b)

Fig.3.4 Calculated strain in the (a) well and (b) barrier.

Fig.3.4.a and Fig.3.4.b show the variations of strain in the well and the barrier as a function of As content of InGaAsP (well). In both of these figures, strain increases with increasing As content of the well.

3.5.2 QT (ts) structure

This type of strain-compensated quantum well structure denotes tensile $In_{1-x}Ga_xAs_yP_{1-y}$ wells with a constant Ga fraction which is taken as 0.55 and compressive $InAs_xP_{1-x}$ barriers.
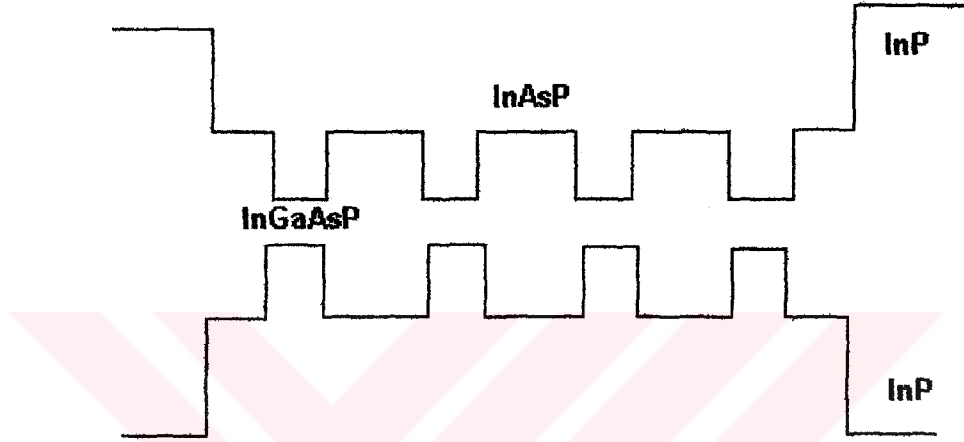
Fig.3.5 Schematic diagram for QT (ts) structure.

The wellwidth and barrier width are fixed at 70Å and 110Å. The number of well is equal to the number of barrier. The As fraction of the well changes from 0.72 to 0.97 to obtain lasing wavelength which varies from 1.27μm to 1.48μm. Barrier content depends on well content by

$$x_b = \frac{(a_s - 5.8688 - \varepsilon_b * 5.8688)}{0.1896 * (\varepsilon_b + 1)} \qquad (3.9)$$

where a_s is the lattice constant of substrate (InP) and ε_b is the strain in the barrier. Equation (3.9) is obtained from Eqn.(3.7) and proof is provided in Appendix B.

Fig.3.6 shows the As content of InAsP (barrier) as a function of As content of InGaAsP (well) to obtain the strain-compensated QT (ts) structure .

22
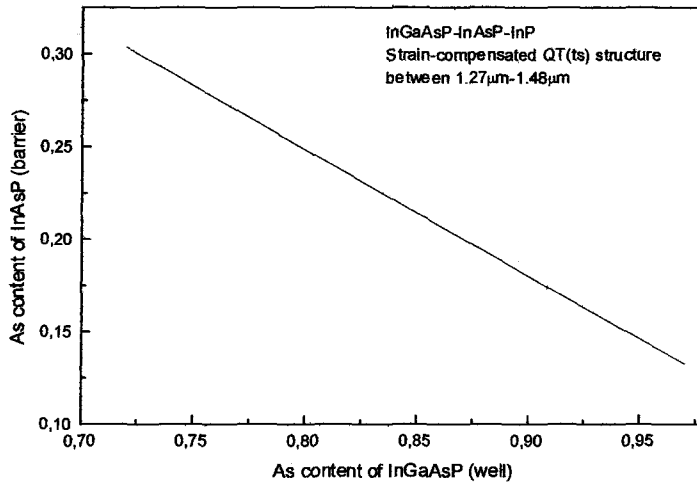
Fig.3.6 The variation of As content of barrier versus As content of well.

This figure has been plotted according to the equation (3.9). In this region, well strain is always tension and barrier strain is compression. Strain of the well changes from 0.67% to 1.52 % and strain of the barrier changes from -0.971% to -0.42% , when the As content of the well changes from 0.72 to 0.97.

(a)

InGaAsP-InAsP-InP
Strain-compensated QT(ts) structure
between 1.27µm-1.48µm

(x-axis: As content of InGaAsP (well); y-axis: Strain in barrier (%))
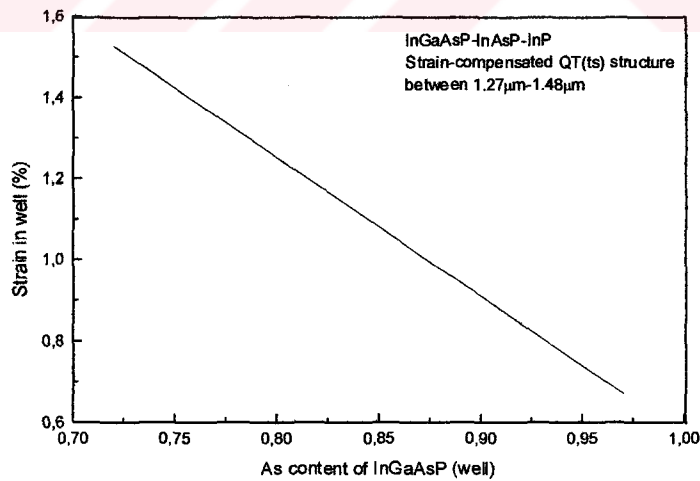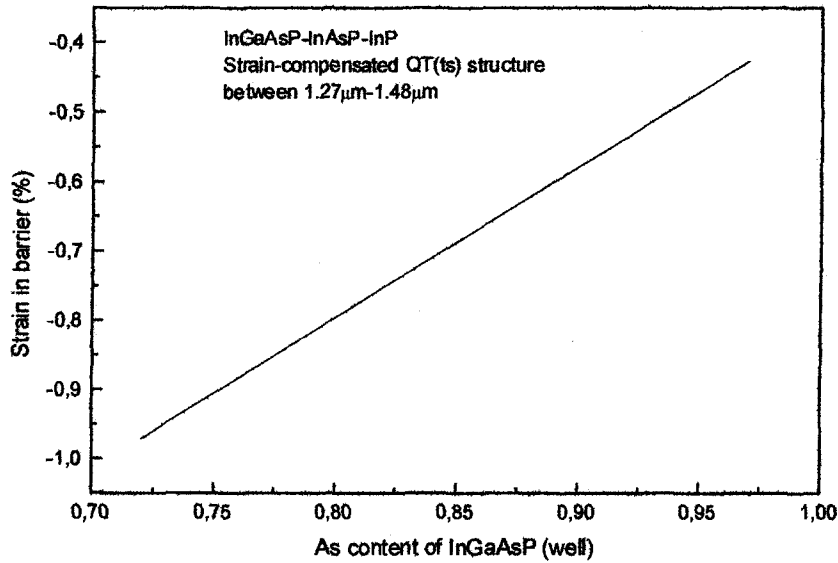
(b)

Fig.3.7   Calculated strain in the (a) well and (b) barrier.

As can be seen from Fig.3.7a and Fig.3.7b that as the magnitude of the strain in the well increases with increasing arsenide concentration, the magnitude of strain in the barrier decreases to satisfy strain compensation.

3.6   Optical Confinement Factor Γ for Multible Quantum Wells

In semiconductor lasers, the ratio of the optical power in the active layer to the total optical power is an important parameter, because it influences the lasing threshold. This ratio is called optical confinement factor Γ and the optical analysis of Γ for single quantum-well laser is conventional in that one solves for the TE modes in a three region dielectric optical waveguides numerically. However, the analysis of Γ for MQW's is not straight forward. Therefore, in this section first we intend to outline the procedure to calculate Γ for multible quantum wells (MQW's) and second, we present the result of the calculations on strain compensated MQW's, and finally, we provide a comparison for different strain compensated structures.

24

3.6.1 The model

The refractive index profile for five-layer symmetric slab waveguide is shown schematically in Fig.3.8. It consists of a central layer, refractive index n_1, thickness 2a, embedded in a cladding layers of index n_2, overall thickness 2b, which are in turn sandwiched between outer claddings of index n_3. For the structure considered here, $n_1 \geq n_2 \geq n_3$. The five-layer guide is symmetric about the midpoint of the core region which is accordingly designated as x=0.
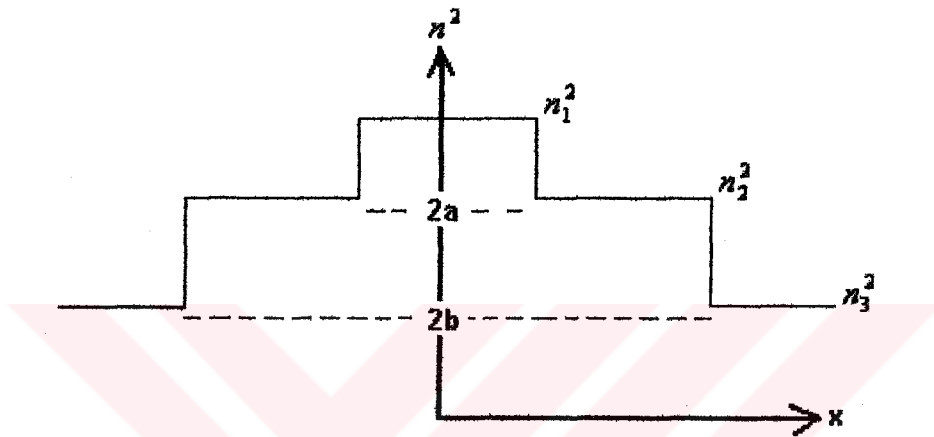
Fig.3.8 The five-layer symmetric slab waveguide.

The thickness a and b can be written for a single QW as

$$a = \frac{(noofw * lw)}{2} \quad , \quad b = \left[\frac{(lw + lb)}{2} \right] * noofw, \qquad (3.10)$$

where $noofw$ is the number of the well, lw is the thickness of the well, and lb is the thickness of the barrier.

In the case of the multible quantum wells (MQW's) one can consider a single quantum well with a total thickness of MQW's and it is splitted up MQW's. So the thickness of the single QW is equal to the thickness of MQW's. This is shown in Fig.3.9a and Fig.3.9b.

25
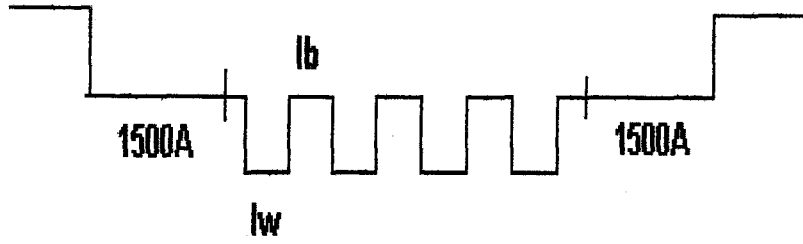
(a)
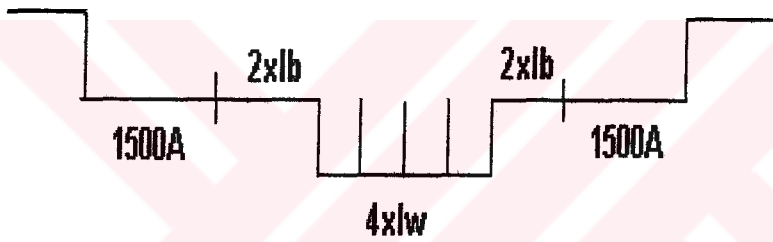
(b)

Fig.3.9   (a) Diagram for 4 QW's, (b) considered as a SQW instead of 4 QW's

Therefore Eqn. (3.10) can be modified as

$$a = \frac{(noofw * lw)}{2} , \qquad b = \left[\frac{2a + noofw * lb + 2 * lc)}{2} \right], \qquad (3.11)$$

where lc is the thickness of the cladding layer which is taken as 1500Å in our calculations. The optical confinement factor Γ is

$$\Gamma = \frac{Gamma1}{Gamma2 + Gamma3 * Gamma4} \qquad (3.12)$$

26

where

$$Gamma1 = u + \sin u * \cos u \qquad\qquad Gamma2 = u + \sin u . \cos u \left(1 - \frac{u^2}{t^2}\right)$$

$$Gamma3 = u * \left(\cos^2 u + \frac{u^2}{t^2}\sin^2 u\right) \qquad Gamma4 = \left(\frac{b}{a} - 1 + \frac{1}{w}\right)$$

$$k = 2\pi/\lambda, \qquad kn_2 \geq \beta \geq kn_3$$

$$v^2 = a^2 k^2 (n_1 - n_3) \qquad\qquad u^2 = a^2 (k^2 n_2^2 - \beta^2)$$

$$w^2 = a^2 (\beta^2 - k^2 n_3^2) = v^2 - u^2 \qquad\qquad t^2 = a^2 (k^2 n_2^2 - \beta^2) = u^2 - v^2 c^2$$

$$c^2 = \frac{n_1^2 - n_2^2}{n_1^2 - n_3^2}$$

$$u = M\pi + \tan^{-1}\left\langle \frac{t}{u}\tan\left[\tan^{-1}\left(\frac{w}{t}\right) - t\left(\frac{b}{a} - 1\right)\right]\right\rangle \quad (M = 0,1,2....). \qquad (3.13)$$

3.6.2 Calculations

(a)

27
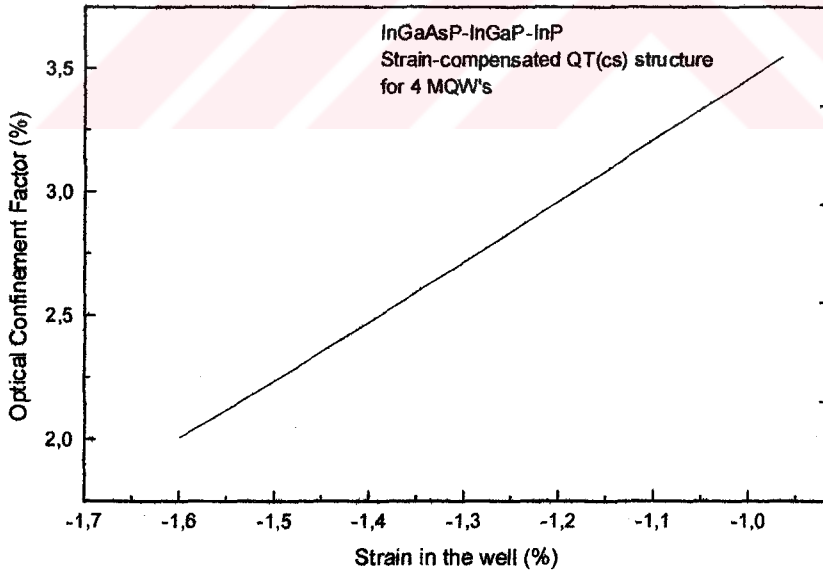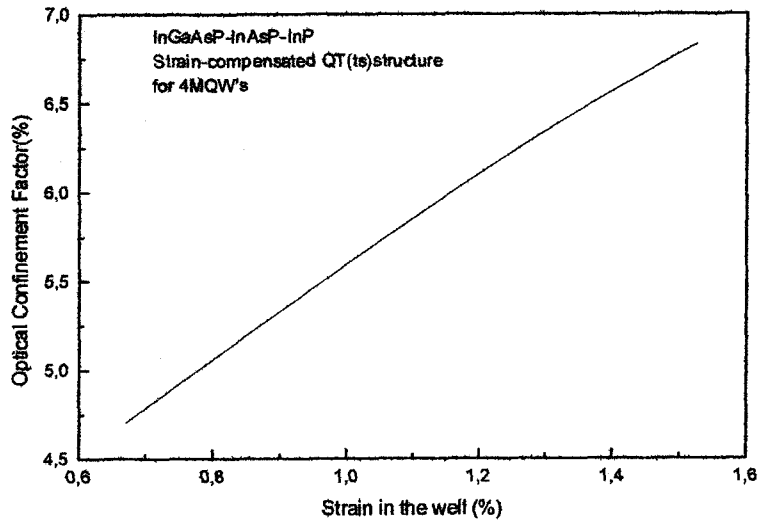
(b)

Fig.3.10 Calculated diagrams of Γ as a function of strain for strain compensated (a) QT(cs) (Fig.3.10a) and (b) QT(ts) (Fig.3.10b) structures.

Fig.3.10 shows the variation of the optical confinement factor as a function of strain in the well for InGaAsP-InGaP-InP strain-compensated QT(cs) and InGaAsP-InAsP-InP strain-compensated QT(ts) structures (Fig.3.10b). Higher optical confinement factor is obtained due to the decrease of strain in the QT(cs) structure. In the QT(ts) structure, the higher optical confinement factor can be observed with increase of the strain in the well.

Optical confinement factor Γ decreases with increasing compressive strain in the QT (cs) case, however Γ increases with increasing tensile strain in the QT(ts) case. The analysis of Fig.3.10 reveals the fact that strain compensated structure with tensile active layers are more effective to increase the performance of devices due to their higher Γ values. The variation in Γ is due to the variations in refractive indices and band gap energies of the corresponding layer. The refractive index n of the medium is related to the energy as

28

$$n = \sqrt{\left(\frac{1 + n_0 * n_d}{n_0^2 - E_0^2} \right)}$$

(3.14)

The n_0 and n_d values can be determined with interpolation method. The corresponding values are provided in Table 3.2 for binary constituents. The refractive index of the well and the barrier are obtained from equation (3.14)
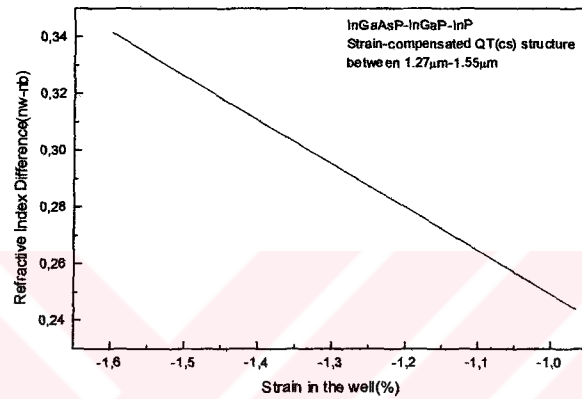
(a)
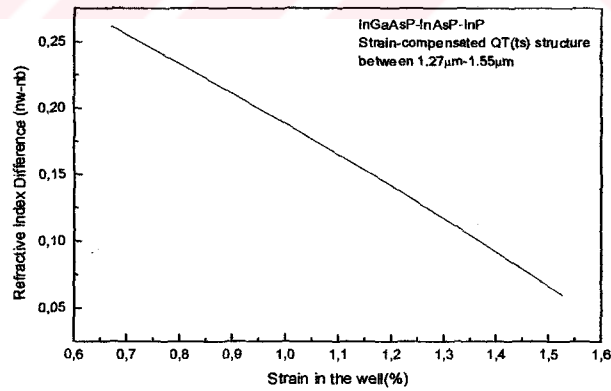
(b)

Fig.3.11 Variation of refractive index difference versus strain in the well for strain-compensated (a) QT(cs) structure and (b) QT(ts) structure.

Fig.3.11a and Fig.3.11b show the refractive index difference (n_w-n_b) as a function of strain in the well for InGaAsP-InGaP-InP strain-compensated QT(cs) and InGaAsP-InAsP-InP strain-compensated QT(ts) structures. In the Fig.3.11a, The refractive index difference increases with increasing strain in the well for QT (cs) structure, see Fig.3.11a. However, refractive index difference decreases with increasing strain in the well for QT(ts) structure, see Fig.3.11b. This opposite behavior is the reason of the trend that we have calculated in Fig.3.10.

Table.3.2   Refractive index values for some binary materials.

Material	n_0	n_d	n
GaAs	3.65	36.1	3.347
InAs	1.5	16.2	3.42
GaP	4.51	36.45	2.90
InP	3.39	28.9	3.1

3.7 Summary

In this chapter we first present the strain theory and the band parameters. Second, we explain how can we obtain a strain-compensated structure and provide the plots of the compensation for the chosen structures. Finally, we examine the optical confinement factor which is an important parameter that determines the threshold gain of the system. During this investigation we offer a model to calculate optical confinement factor for multible quantum wells. Our calculations demonstrate that higher values of optical confinement factor can be obtained in the case of tensile active layers which are compensated with compressively strained barriers.

CHAPTER 4

MODEL BAND-OFFSET CALCULATIONS FOR
STRAIN COMPENSATED STRUCTURES

4.1 Introduction

Strain provides another degree of freedom to tailor the band structure of quantum well (QW) structures and improves the performance of optoelectronic devices compared to those with lattice-matched QW structures. Devices with strained active layer have been designed and fabricated with enhanced performance [20-23]. While the total thickness of the strained layers without defect generation during the growth is limited by a critical thickness, by strain compensating with the opposite strain in the barrier, the number of the quantum wells can be increased. Furthermore, strain compensation gives us another way to modify the material compositions, which is essential to tailoring the band structure. Strain compensation has recently been used in many device structures, such as QW lasers and modulators, most of which show better performance than strain-uncompensated structures [24-28].

In order to design and fabricate high performance devices, one should optimise the band structure. When modelling the band structure for a QW, the relative alignment of the band edges of the well and barrier material is very important. The determination of strain-dependent band-offsets at the interface of the ternary and quaternary material is one of the major obstacles while modelling the band structure since there are only few data for arbitrary compositions of the material systems used in our structures, especially for the strained cases. In this chapter we

31

present and compare two models for the band alignment of the strain compensated systems.

4.2 Calculation of Bulk Bandgap with Strain

For our model the average valance-band energy hydrostatic deformation potentials are obtained for the constituent binary compounds. The bandgap, spin-orbit splitting, and the parameters for calculating the shear deformation potential are obtained from the corresponding experimental data of the binary compounds. Then, an interpolation scheme of expanding the material parameters of ternary and quaternary alloys in fractional constituent ratio x (and/or y) is used to determine the band parameters for lattice matched and strained heterostructures. The interpolation formulas for all physical parameters P used in the calculation of $In_{1-x}Ga_xAs_yP_{1-y}$, $In_xGa_{1-x}P$ and $InAs_xP_{1-x}$, are given as

$$P(In_{1-x}Ga_xAs_yP_{1-y}) = P(GaAs)xy + P(GaP)x(1-y) + P(InAs)(1-x)y \quad (4.1)$$
$$+ P(InP)(1-x)(1-y)$$

$$P(In_{1-x}Ga_xP) = P(GaP)x + P(InP)(1-x) \quad (4.2)$$

$$P(InAs_xP_{1-x}) = P(InAs)x + P(InP)(1-x) \quad (4.3)$$

The material parameters of the binary semiconductors can be found in Table 4.1. The exception to the linear interpolation is the formula for the unstrained bandgap. For $In_{1-x}Ga_xAs_yP_{1-y}$, this quantity is given as

$$E_g(x, y) = 1.35 + 0.642\,x - 1.101\,y + 0.758\,x^2 + 0.101\,y^2 \quad (4.4)$$
$$- 0.159\,xy - 0.28\,x^2y + 0.109\,xy^2$$

The effects of the strain are calculated in the following way. First, the strain in the plane of the epitaxial growth is

$$\varepsilon = \varepsilon_{xx} = \varepsilon_{yy} = \frac{a_0 - a}{a} \quad (4.5)$$

32

where a is the lattice constant of the quaternary epitaxial layer and a_0 is the lattice constant of the substrate which is assumed to be InP. The strain in the perpendicular direction can be expressed as

$$\varepsilon_{zz} = -2\frac{C_{12}}{C_{11}}\varepsilon \qquad (4.6)$$

where C_{11} and C_{12} are elastic stiffness constants. The conduction band is shifted by the energy

$$\delta E_c(x,y) = a_c(\varepsilon_{xx} + \varepsilon_{yy} + \varepsilon_{zz}) = 2a_c\left(1 - \frac{C_{12}}{C_{11}}\right)\varepsilon \qquad (4.7)$$

and valence bands are shifted by

$$\delta E_{hh}(x,y) = -P_\varepsilon - Q_\varepsilon \qquad (4.8)$$

$$\delta E_{lh}(x,y) = -P_\varepsilon + Q_\varepsilon \qquad (4.9)$$

where

$$P_\varepsilon = -a_v(\varepsilon_{xx} + \varepsilon_{yy} + \varepsilon_{zz}) = -2a_v\left(1 - \frac{C_{12}}{C_{11}}\right)\varepsilon \qquad (4.10)$$

$$Q_\varepsilon = -\frac{b}{2}(\varepsilon_{xx} + \varepsilon_{yy} - 2\varepsilon_{zz}) = -b\left(1 + 2\frac{C_{12}}{C_{11}}\right)\varepsilon \qquad (4.11)$$

where a_c and a_v are the conduction-band and valence-band hydrostatic deformation potentials, and b is the valence –band shear deformation potential.

The strained bandgaps can then be expressed as

$$E_{c-hh}(x,y) = E_g(x,y) + \delta E_c(x,y) - \delta E_{hh}(x,y) \qquad (4.12)$$

and

33

$$E_{c-lh}(x,y) = E_g(x,y) + \delta E_c(x,y) - \delta E_{lh}(x,y) \qquad (4.13)$$

Table 4.1 Parameters for the calculation of strain and bandgap energy.

Parameters	Symbol	GaAs	InAs	InP	GaP
Bandgap Energy	E_0(e.V)	1.42	0.36	1.35	2.74
Lattice constant	a(Å)	5.6533	6.058	5.868	5.450
Elastic Stiffness Constant	$C_{11}(10^{11}$dyn/cm$^2)$	11.879	8.329	10.11	14.05
Elastic Stiffness Constant	$C_{12}(10^{11}$dyn/cm$^2)$	5.376	4.526	5.61	6.203
Hydrostatic deformation potential For Conduction band	a_c(eV)	-7.17	-5.08	-5.04	-7.14
Hydrostatic deformation potential for Valence band	a_v(eV)	1.16	1.00	1.27	1.70
Shear deformation potential for valence band	b_v(eV)	-1.7	-1.8	-1.7	-1.8
Valence band paremeter	γ_1	6.8	20.4	4.95	4.05
	γ_2	1.9	8.3	1.65	0.49
	γ_3	2.73	9.1	2.35	1.25
Electron effective mass	m_c/m_0	0.067	0.023	0.077	0.25
Heavy-hole effective mass	m_{hh}/m_0	0.5	0.40	0.60	0.67

4.3 Theoretical Models for the Calculation of Bandoffsets

The relative alignment of the band edges of the well and barrier material is very important in modelling the band structure. Since experimental measurements for the band offsets in strained QW's remain very difficult, scarce, and uncertain, a theoretical approach must be used to obtain physical reasonable estimations of material parameters for strained QW's. In this section we present two methods of Model Solid Theory and Harrison's model. With these methods, the band offsets of strained QW's in ternary and quaternary systems are obtainable rather than from empirical extrapolations of rarely available, scattered and often indirect experimental data for quaternary compounds.

34

A. Model Solid Theory [29], [30]: The valence band position of a quaternary is given by

$$E_v(x,y) = E_{v,av}(x,y) + \frac{\Delta(x,y)}{3} + \delta E_{hh}(x,y) \qquad \text{for hh (compressive strain)}$$

(4.14)

$$E_v(x,y) = E_{v,av}(x,y) + \frac{\Delta(x,y)}{3} + \delta E_{lh}(x,y) \qquad \text{for lh (tensile strain)}$$

(4.15)

where $E_{v,av}(x,y)$ is the average valence subband energy and Δ is the spin-orbit split-off band energy. These values are obtained by a linear interpolation of the binary values listed in Table 4.2. The conduction band position may be calculated by simply adding the strained bandgap energy to the valence band position

$$E_c(x,y) = E_v(x,y) + E_{c-hh}(x,y) \qquad \text{for hh (compressive strain)}$$

(4.16)

$$E_c(x,y) = E_v(x,y) + E_{c-hh}(x,y) \qquad \text{for lh (tensile strain)}$$

(4.17)

Table 4.2   Parameters for the calculation of strain and band gap energy for $In_{1-x}Ga_xAs_yP_{1-y}$.

Parameter	Symbol	GaAs	InAs	InP	GaP
Model solid theory: Average valence band position	$E_{v,av}(eV)$	-6.92	-6.67	-7.04	-7.40
Model solid theory: Spin-Orbit split-off energy	$\Delta(eV)$	0.34	0.38	0.11	0.08
Harrison model: Conduction band position	$E_c^H(eV)$	1.53	0.801	1.35	2.352
Harrison model: Valence band position	$E_v^H(eV)$	0.111	0.441	0.00	-0.388

35

The conduction band offset is given by

$$\frac{\Delta E_c}{\Delta E_g} = 1 - \frac{E_v^w - E_v^b}{E_g^b - E_g^w} \qquad (4.18)$$

where E_v^w and E_v^b are the valence band positions in the well and barrier materials, respectively, and E_g^w and E_g^b are the strain adjusted band gaps ($E_{c\text{-}hh}$ for compressive strain and $E_{c\text{-}lh}$ for tensile strain) for the well and barrier materials.

B. Harrison's Model [31]: The position of both the conduction and valence bands are determined by

$$E_v(x, y) = E_v^H(x, y) + \delta E_{hh}(x, y) \qquad \text{for hh (compressive strain)} \qquad (4.19)$$

$$E_v(x, y) = E_v^H(x, y) + \delta E_{hh}(x, y) \qquad \text{for lh (tensile strain)} \qquad (4.20)$$

$$E_c(x, y) = E_c^H + \delta E_c(x, y) \qquad (4.21)$$

where $E_v^H(x,y)$ and $E_c^H(x,y)$ are obtained by a linear interpolation of the binary parameters found in Table 4.2 [19], and $\delta E_{hh}(x,y)$, $\delta E_{lh}(x,y)$, and $\delta E_c(x,y)$ are the strain-induced energy shifts given in (4.7)-(4.9). The superscript 'H' refers to Harrison's model. The conduction band-edge discontinuity may then be calculated as

$$\frac{\Delta E_c}{\Delta E_g} = \frac{E_c^{H.b} - E_c^{H.w}}{(E_v^{H.w} - E_v^{H.b}) + (E_c^{H.b} - E_c^{H.w})} \qquad (4.22)$$

where the superscripts w and b indicate the well and barrier materials, respectively.

It should be noted that this method simply is meant to give the parameter $\Delta E_c/\Delta E_g$ which may be used to determine the alignment of the well and barrier materials. The difference between $E_c(x,y)$ and $E_v(x,y)$ from equation (4.19), (4.20) and (4.21) should not be used to calculate the bandgap of the quarternary material. Rather, equation (4.4) should be used.

36

4.4 The Computed Results and Comparison

This section presents the band-offset values for our laser structures using Model Solid Theory and Harrison Model.

4.4.1 Strain-compensated QT(cs) structure

A comparison of the model-solid theory and Harrison model for the calculation of the conduction band offset ratio for strain compensated InGaAsP/InGaP/InP structure with compressively strained active layers is shown in Fig.4.1
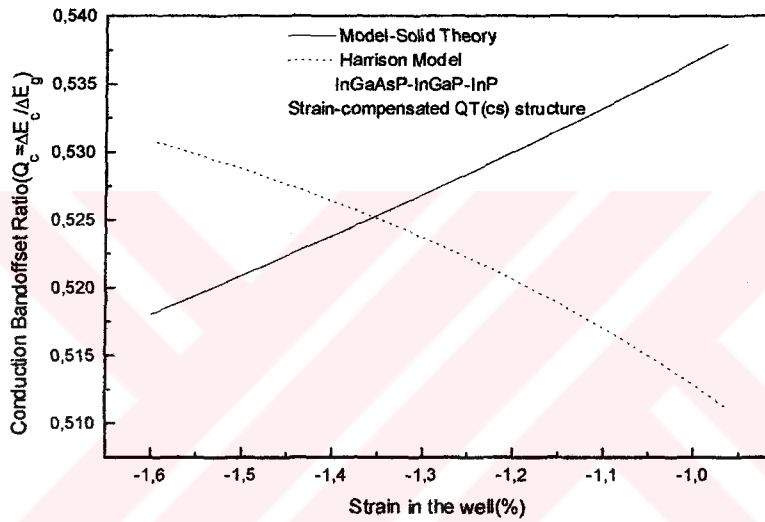
Fig.4.1 Diagram for conduction bandoffset ratio versus strain in the well for QT(cs) structure.

The variation of the conduction bandoffset ratio $Q_c=\Delta E_c/\Delta E_g$ versus strain in the well for the InGaAsP-InGaP-InP strain-compensated QT(cs) structure displays an opposite trend for each model, i.e., conduction band offset ratio increases with increasing strain according to the Harrison model however conduction band offset ratio decreases with increasing strain according to the Model Solid Theory. The experimental results [Minch et. al.] for $In_{1-x}Ga_xAs_yP_{1-y}$ system show similar trends to that of the Harrison model, therefore Harrison model is reliable for this material system.
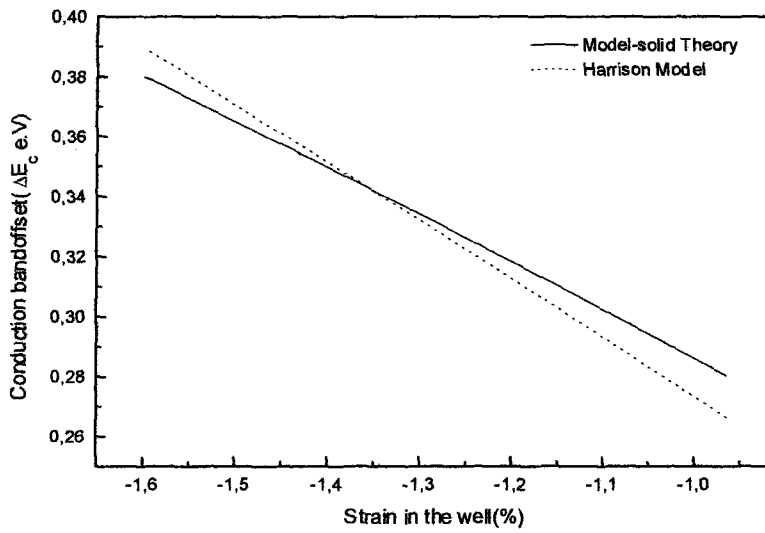
(a)
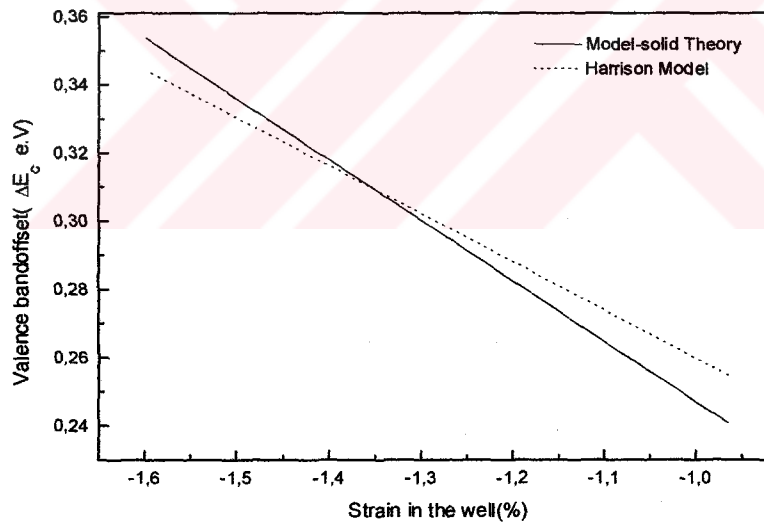
(b)

Fig.4.2 The variation of (a) conduction band offset ΔE_c and (b) valence band offset ΔE_v according to the two models.

38

Fig.4.2a and Fig.4.2b show the diagrams for the conduction bandoffset ΔE_c and valence bandoffset ΔE_v versus strain in the well for the QT(cs) structure according to the Model-solid theory and Harrison's model. In both of these figures, conduction and valence band offsets decrease with decreasing strain in the well. This causes shallow well in the valance band, which reduces the hole escape time from the wells.

4.4.2 Strain-compensated QT(ts) structure

Fig.4.3 shows a comparison of Model-solid theory and Harrison model in the case of InGaAsP/InAsP/InP with tensile active layers. An opposite trend similar to that of the Fig.4.1 is obtained.
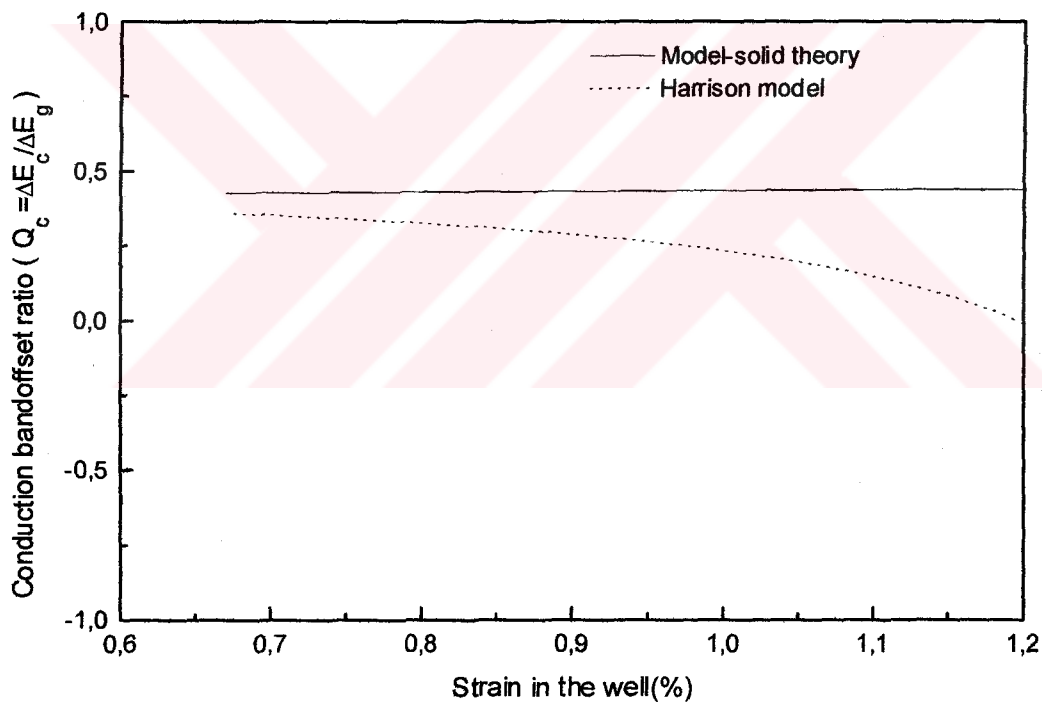
Fig.4.3 Conduction bandoffset ratio Q_c, versus strain in the well
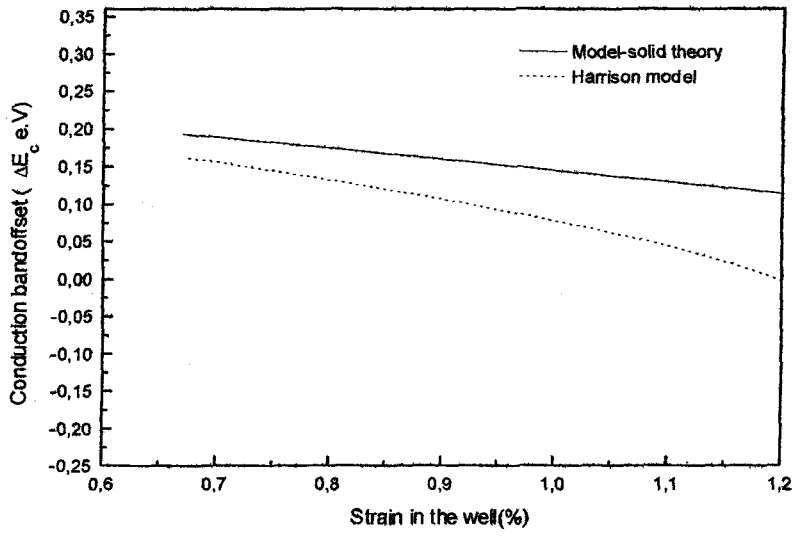
(a)
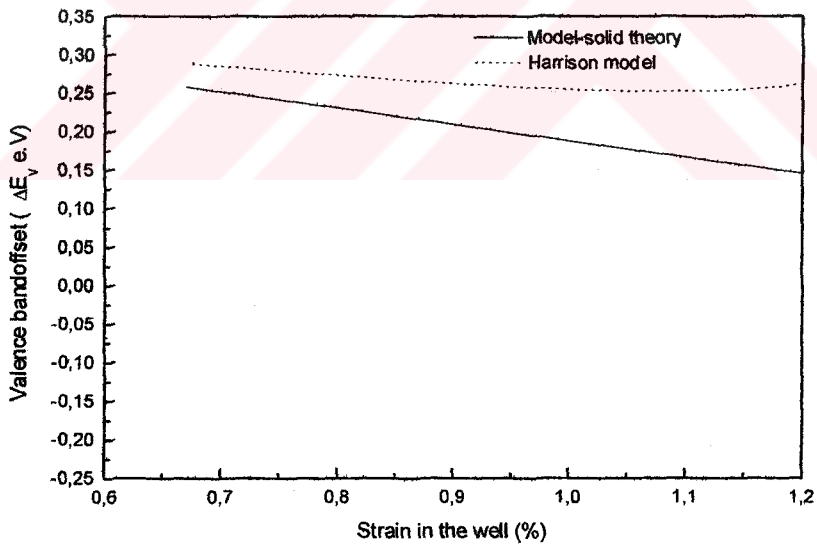
(b)

Fig.4.4 The variation of (a) conduction band offset ΔE_c and (b) valence band offset ΔE_v according to the two models.

In Fig.4.4a and Fig.4.4.b, the conduction band-offset ΔE_c and valence bandoffsets ΔE_v has been plotted according to the strain in the well for InGaAsP-InAsP-InP QT(ts) structure. There is a decrease in the conduction and valance bandoffset when strain increases. Deep wells cause an increase in the absorption coefficient and make the device operate at a lower voltage. While optimizing the strain-compensated structures one needs to take into consideration the fact that the deep electron wells are essential for achieving good high temperature laser performance. This suggests that well strain should be kept at lower values while optimizing the strain compensated systems.

4.5 Allowed Energy Levels in QW

The number of the allowed energy levels and the separation between these levels are important issues which have to be addressed during modeling the strain compensated laser structures. Therefore, it is our aim at this point to discuss the influence that this has on design issues. In following subsections the conduction and valence band structures are obtained for our laser structures.

4.5.1 Strain-compensated QT(cs) structure

(a)

41
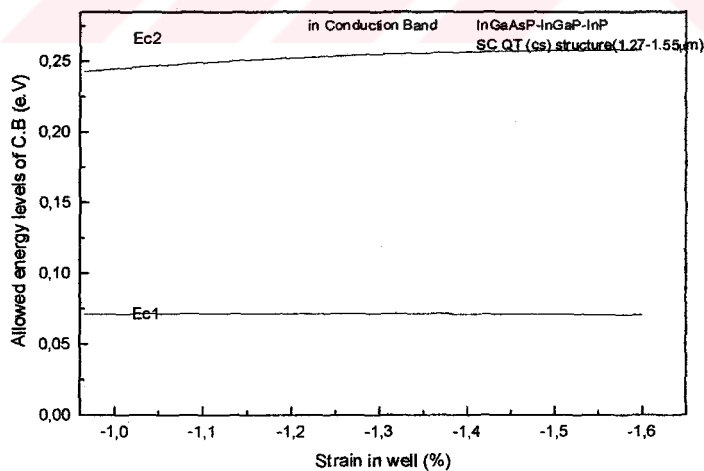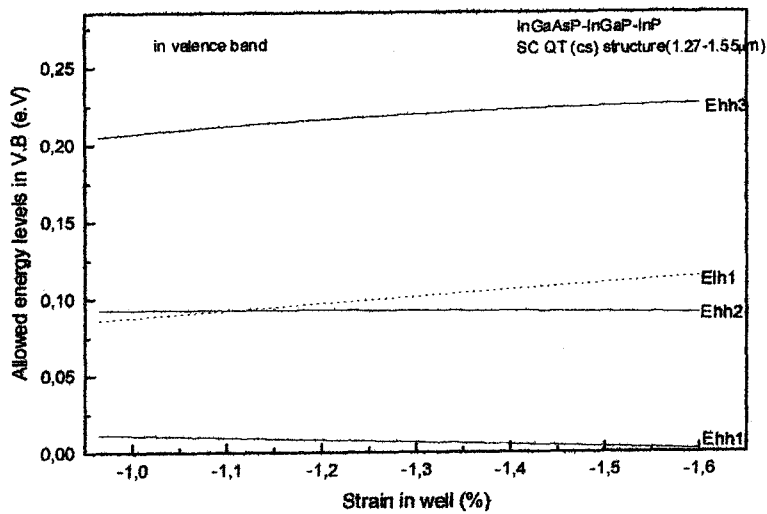
(b)

Fig.4.5 Allowed energy levels in (a) conduction band (b) valence band for QT(cs) structure.

The allowed energy levels in conduction band and valence band are shown in Fig.4.5. There is almost no change in confined energy levels in conduction band with increasing strain. Minor variations with increasing strain of confined levels in valence band are calculated and shown in Fig.4.5b.

4.5.2 Strain-compensated QT(ts) structure

Fig.4.6 shows the allowed energy levels in conduction band (see in fig.4.6a) and valence band (in fig.4.6b). It can be seen from Fig.4.6a that the confined levels get closer with increasing strain, which brings a disadvantage for device designing due to its negative effect on subband carrier populations. The same conclusions can also be derived for the confined energy levels in valence band. Therefore, the route of low strain should be followed when designing an emitter by means of strain compensation.

42
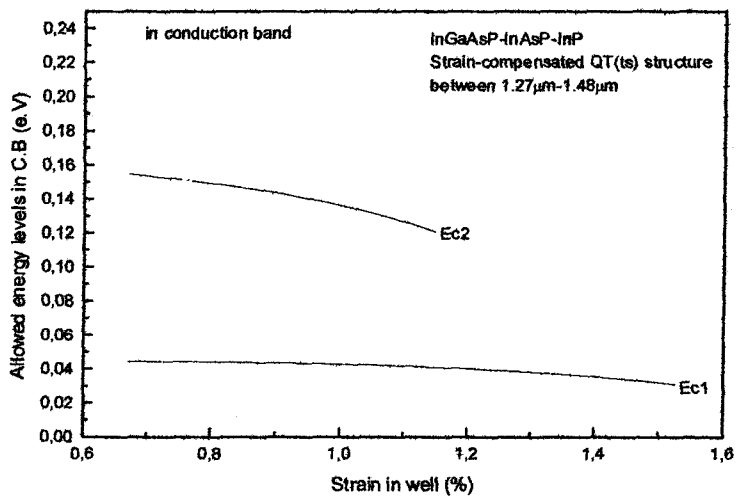
(a)
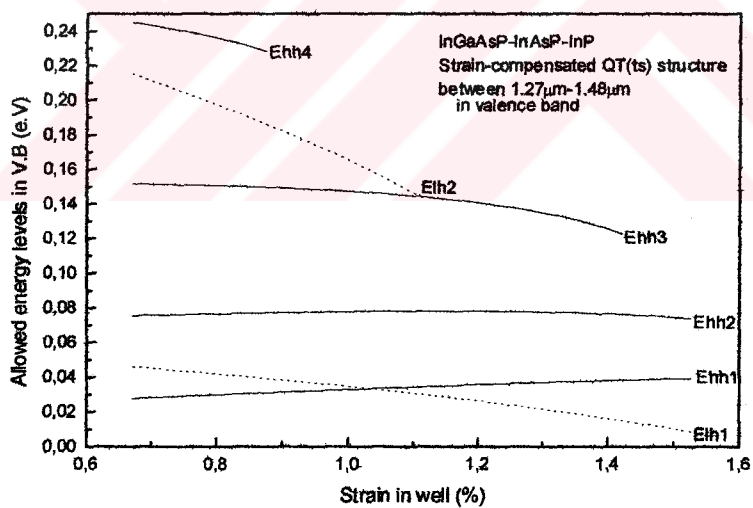
(b)

Fig.4.6 Allowed energy levels in (a) conduction band (b) valence band for QT(ts) structure.

4.6 Conclusions

We present band-offset ratios for our strain-compensated laser structures using Model Solid Theory and Harrison model. The trend that we have obtained using Harrison model is in agreement with experimental values. The comparison of valence and conduction band-offset's for the two laser structures reveals the fact that the wells are deeper in the case of compressively strained active layers than that of tensiley strained active layers in strain-compensated structures. The deep wells provide good quantum confinement which is beneficial for device designing.

We also make a comparison of the confined levels in conduction and valence band of the related strain-compensated structures. Ideally one would like to achieve as small numbers as possible in both conduction and valence band. The level separation would be as high as possible. Keeping in mind these requirements, strain compensated QT(cs) structure gives better results than that of strain compensated QT(ts) structure. As an overall, our calculated results shows that strain compensated QT(cs) structure can show better device performance compared to strain compensated QT(ts) structure. However, for laser applications QT(ts) system has several important advantages. First of all, a better high temperature performance of the laser structures can be achieved due to its larger band-offset and, thus, improved carrier confinement and decreased carrier spill out at RT and above. Secondly the less number of confined levels and the large energy separation between them lead to achieve the transparency carrier density at lower injected carrier density due to the positive effect on subband carrier populations which is a great benefit for lasers.

CHAPTER 5

THE COMPARISON STRAIN COMPENSATED AND UNCOMPENSATED STRUCTURES

5.1 Introduction

Several reports on 1300 nm laser structures with strained wells and lattice-matched barriers have been published [32-34]. However, the number of quantum wells for this applications is often limited and reports on strain-compensated 1300 nm structures are therefore of great interest [35,36]. Silfvenius et. al. [28] have introduced different concepts for achieving strain-compensated quantum well structures emitting at 1300 nm. They have shown that structures employing up to eight compressively strained wells with the same x in well and barrier exhibits excellent structural and optical properties, including very high photoluminescence efficiency. They were demonstrated good laser characteristics for strain-compensated structures with tensile wells.

As has been stated before, some authors [4,7] have reported that strain-compensated quantum wells could offer higher gain and higher differential gain than more conventional compressively strained quantum wells. Therefore it is our aim at this point to clear out the reasons behind such a behavior. This will be done by calculating the band structure parameters for the chosen strained-compensated structures and their more conventional compressively strained correspondings. The comparison are provided in the sections.

5.2 Band Parameters

Using the Harrison's model we obtain the average valence-band energy and hydrostatic deformation potentials in terms of the constituent binary compounds. The bandgap and the parameters for calculating the shear deformation potential are obtained for ternary and quarternary materials by means of an interpolation scheme. The band offsets of strained quantum wells in ternary and quarternary system are obtained using Harrison's model. The strain dependent, anisotropic effective masses of the HH and LH bands are determined using Eqn's (3.2) and (3.3). The effective mass of the conduction band is determined via linear interpolation of the corresponding binary constituents.

5.3 Model

The band-edge peak gain for electron and hole carrier density n at the QW band edge is given by [37]

$$G_{max} = G_0(1 - e^{-n/n_C} - e^{-n/n_V})$$ (5.1)

with

$$G_0 = \frac{\Gamma E_g \mu^2 m_r}{\varepsilon_0 c \eta \hbar^3 L_z}, \qquad n_{c,v} = \frac{m_{c,v}}{\pi \hbar^2 L_z} kT$$ (5.2)

where E_g is the optical energy gap, μ^2 is the squared dipole moment along a given polarisation of light, m_r is the reduced mass, ε_0 is the permittivity in vacuum, η is the refractive index of the material, and L_z is the well width. Transparency occurs when $G_{max}=0$, and the transparency carrier density n_{tr}, required for population inversion, can be found by solving equation (5.1) as

$$1 - e^{-\alpha} = e^{-\alpha/R}$$ (5.3)

where

$$\alpha = n_{tr}/n_v, \qquad \text{and} \qquad R = m_c/m_v$$ (5.4)

46

The differential material gain at transparency, $\beta=dG_{max}/dn$, can be determined by differentiating the peak gain in equation (5.1) with respect to carrier density as [37]

$$\beta = \frac{\beta_0 E_g}{1+R}\left[1+e^{-\alpha}(R-1)\right],$$

(5.5)

with

$$\beta_0 = \frac{\mu^2 \pi}{\varepsilon_0 cn\hbar kT}.$$

(5.6)

We assume a linear relationship between carrier density n and the peak laser gain g, so that the threshold carrier density, n_{th}, is then given by

$$n_{th} = n_{tr} + \frac{g_{th}}{\beta},$$

(5.7)

where g_{th} is the threshold material gain which takes the form

$$g_{th} = \alpha_a + \frac{1-\Gamma}{\Gamma}\alpha_c + \frac{1}{\Gamma L}\ln\left(\frac{1}{R}\right)$$

(5.8)

where α_a and α_c are the active layer and cladding layer losses, L is the length of the laser and R is the reflectivity of the end mirrors.

5.4 QT(cs) Structure at 1.29μm Wavelength

Tensile strained InGaP barriers and compressively strained InGaAsP quantum wells are one means for achieving strain compensation. Fig.5.1a shows such a strain compensated structure, four 50-Å-thick $In_{0.89}Ga_{0.11}As_{0.56}P_{0.44}$ QW active layers (wells) surrounded by 94-Å-thick $In_{0.92}Ga_{0.08}P$ barrier layers. The active layer structure is sandwiched between InP cladding layers. In this structure, wells are under compression strain and barriers are under tension strain. The wavelength is 1.29μm [28]. We have chosen a corresponding uncompensated structure emitting at 1.29μm to compare with compensated structure. This structure is shown in Fig.5.1b.

This structure consist of four $In_{0.89}Ga_{0.11}As_{0.54}P_{0.46}$ quantum wells and $In_{0.746}Ga_{0.254}As_{0.55}P_{0.45}$ barriers which are lattice matched to InP. In this structure, wells are under compression strain and barriers are lattice-matched to substrates.

(a)

(b)

Fig.5.1   Schematic diagram of (a)   QT(cs) compensated structure (b)   QT(cs) uncompensated structure

The calculated parameters for both of these structures have been provided in Table 5.1.

Table5.1 Parameters for QT(cs) strain-compensated and QT(cs) uncompensated structures.

QT(cs) structures at 1.27μm		
	Strain-compensated structure	**Uncompensated structure**
Well	$In_{0.89}Ga_{0.11}As_{0.56}P_{0.44}$	$In_{0.89}Ga_{0.11}As_{0.54}P_{0.46}$
Barrier	$In_{0.92}Ga_{0.08}P$	$In_{0.746}Ga_{0.254}As_{0.55}P_{0.45}$
Substrate	InP	InP
ε_w **(%)**	-1.028	-0.965
ε_b **(%)**	0.547	0
E_{gw}**-strained (e.V)**	0.8614	0.8799
E_{gb}**-strained (e.V)**	1.404	1.112
Q_c	0.535	0.72
$E_{splitting}$ **(e.V)**	0.036	0.033
ΔE_c **(e.V)**	0.290	0.167
ΔE_v **(e.V)**	0.252	0.65
E_{c1} **(meV)**	71	60
E_{c2} **(meV)**	245	-
E_{hh1} **(meV)**	28	18
E_{lh1} **(meV)**	71	43
E_{hh2} **(meV)**	110	61
E_{hh3} **(meV)**	226	-
E_{0w} **(optical (e.V))**	0.9613	0.9588
n_w	3.445	3.43
n_b	3.19	3.38
n_c	3.1	3.1
λ **(μm)**	1.29	1.29
O.C.F (%)	3.38	5.2
N_v**(cm^{-3})**	1.26031×10^{24}	1.2964638×10^{24}
N_{tr}**(cm^{-3})**	1.12246×10^{24}	1.1274266×10^{24}
G_{th}**(cm^{-1})**	42.4718	40.737
N_{th}**(cm^{-3})**	1.122×10^{24}	1.127×10^{24}

5.5 QT(ts) Structure at 1.33μm Wavelength

Compressively strained InGaP barriers and tensiley strained InGaAsP quantum wells are another way of achieving strain compensation. Therefore, this section provides a comparison of strain-compensated and uncompensated structures in the case tensile active layers. The schematic diagrams are given in Fig.5.2. Fig.5.2a shows the QT(ts) strain compensated structure with four 70-Å-thick $In_{0.55}Ga_{0.45}As_{0.81}P_{0.19}$ QW active layers (wells) surrounded by 110-Å-thick $In_{0.24}Ga_{0.76}P$ barrier layers. The active layer structure is sandwiched between InP cladding layers. In this structure, wells are under tensile strain and barriers are under compression strain. The wavelength is 1.33μm [32]. We have chosen a corresponding uncompensated structure at 1.33μm to compare with compensated structure. This structure is shown in Fig.5.2b. The structure consist of four $In_{0.55}Ga_{0.45}As_{0.76}P_{0.24}$ quantum wells and $In_{0.746}Ga_{0.254}As_{0.55}P_{0.45}$ barriers which are lattice matched to InP. In this structure, wells are under tension strain and there is no strain in the barriers.

(a)   (b)
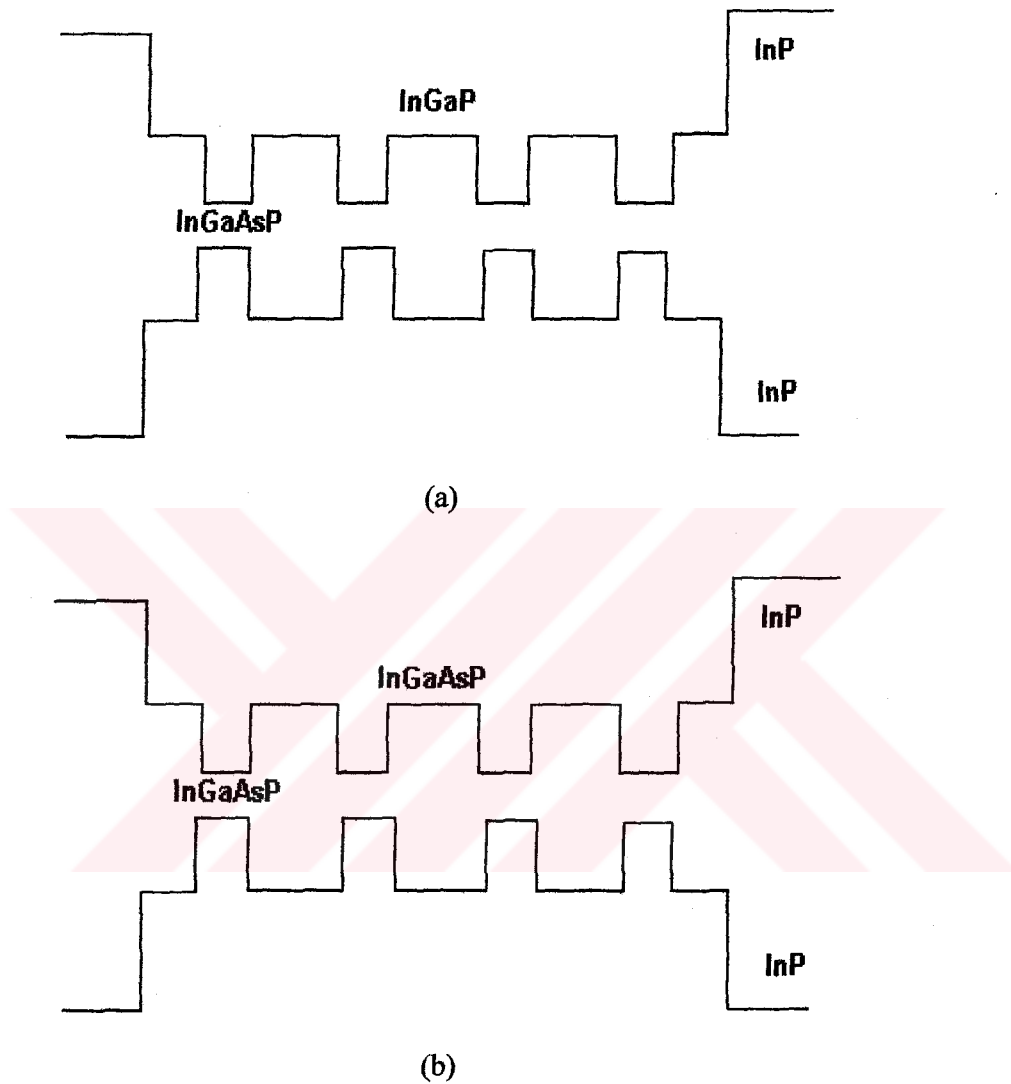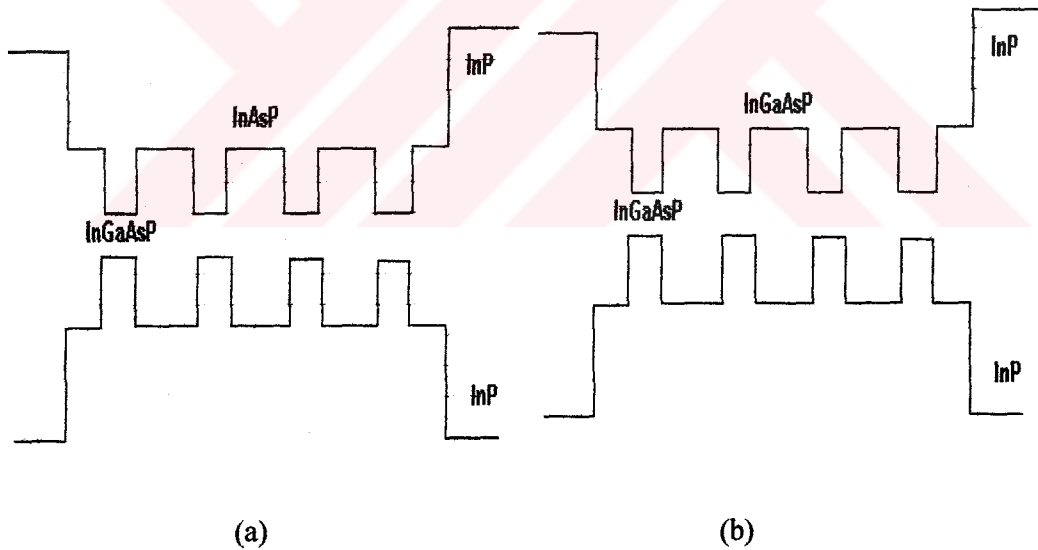
Fig.5.2   Schematic diagram of (a) QT(ts) compensated structure (b) QT(ts) uncompensated structure

The parameters for both of these structures have been tabulated in Table 5.2.

Table.5.2 Parameters for QT(ts) strain-compensated and QT(ts) uncompensated structures

QT(ts) structures at 1.33µm		
	Strain-compensated structure	**Uncompensated structure**
Well	$In_{0.55}Ga_{0.45}As_{0.81}P_{0.19}$	$In_{0.55}Ga_{0.45}As_{0.76}P_{0.24}$
Barrier	$In_{0.24}Ga_{0.76}P$	$In_{0.746}Ga_{0.254}As_{0.55}P_{0.45}$
Substrate	InP	InP
ε_w **(%)**	1.216	0.678
ε_b **(%)**	-0.774	0
E_{gw}**-strained (e.V)**	0.8723	0.8719
E_{gb}**-strained (e.V)**	1.126	1.112
Q_c	0.44	0.87
$E_{spllitting}$ **(e.V)**	-0.042	-0.023
ΔE_c **(e.V)**	0.111	0.210
ΔE_v **(e.V)**	0.142	0.030
E_{c1} **(meV)**	39	46
E_{c2} **(meV)**	-	168
E_{hh1} **(meV)**	14	9
E_{lh1} **(meV)**	46	20
E_{hh2} **(meV)**	56	28
E_{hh3} **(meV)**	118	-
E_{0w} **(optical (e.V))**	0.9267	0.9281
n_w	3.42	3.425
n_b	3.28	3.37
n_c	3.1	3.1
λ **(µm)**	1.33	1.33
O.C.F (%)	6.1	6.96
N_v**(cm^{-3})**	2.1954×10^{24}	$2.10278049 \times 10^{24}$
N_{tr}**(cm^{-3})**	1.0605×10^{24}	1.075277×10^{24}
G_{th}**(cm^{-1})**	345.8612	280.687
n_{th}**(cm^{-3})**	1.06005×10^{24}	1.075277×10^{24}

5.6 Ternary (cs) Structure at 0.96μm Wavelength

Another way of achieving strain compensation is to use tensiley strained ternary GaAsP barriers and compressively strained ternary InGaAs quantum wells. This will be our last comparison of compensated and uncompensated structures. Their schematic diagram is shown in Fig.5.3. Dutta et al. [4] have studied and obtained some parameters related to these structures. Fig.5.3a shows the ternary(cs) strain compensated structure, four 60-Å-thick $In_{0.2}Ga_{0.8}As$ QW active layers (wells) surrounded by 125-Å-thick $GaAs_{0.8}P_{0.2}$ barrier layers. The active layer structure is sandwiched between $In_{0.484}Ga_{0.516}P$ cladding layers. The $In_{0.484}Ga_{0.516}P$ layers are lattice matched to GaAs. In this structure, wells are under compression strain and barriers are under tensile strain. The wavelength is 0.96μm. A corresponding uncompensated structure has been chosen emitting at 1.33μm for comparison [4]. This structure is shown in Fig.5.3b. It consist of four $In_{0.2}Ga_{0.8}As$ quantum wells and GaAs barriers. In this structure, wells are under compression strain and barriers is unstrained.
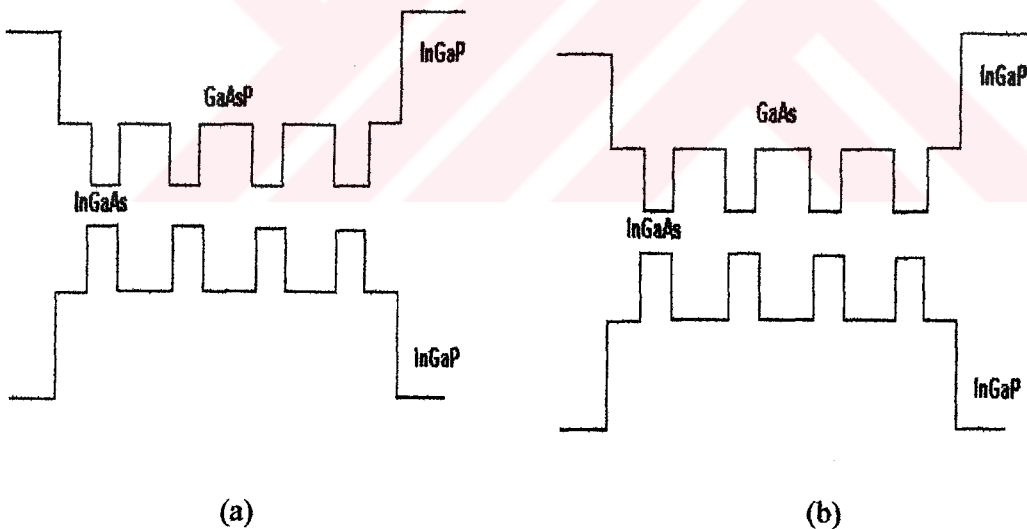

(a)

(b)

Fig.5.3 Schematic diagram of (a) Ternary(cs) strain-compensated (b) Ternary(cs) uncompensated structure

The parameters of both of two structures have been obtained and tabulated in Table 5.3.

Table.5.3 Parameters for Ternary(cs) compensated and Ternary(cs) uncompensated structures.

Ternary(cs) structures at 0.96μm		
	Strain-compensated structure	Uncompensated structure
Well	$In_{0.2}Ga_{0.8}As$	$In_{0.2}Ga_{0.8}As$
Barrier	$GaAs_{0.8}P_{0.2}$	GaAs
Cladding layer	$In_{0.484}Ga_{0.516}P$	$In_{0.484}Ga_{0.516}P$
ε_w (%)	-1.41	-1.41
ε_b (%)	0.678	0
E_{gw}-strained (e.V)	1.219	1.219
E_{gb}-strained (e.V)	1.5837	1.42
Q_c	0.56	0.58
$E_{spllitting}$ (e.V)	0.048	0.048
ΔE_c (e.V)	0.206	0.118
ΔE_v (e.V)	0.157	0.082
E_{c1} (meV)	57	49
E_{c2} (meV)	203	-
E_{hh1} (meV)	18	15
E_{lh1} (meV)	49	36
E_{hh2} (meV)	71	57
E_{hh3} (meV)	145	-
E_{0w} (optical (e.V))	1.294	1.28
n_w	3.59	3.58
n_b	3.42	3.505
n_c	3.2	3.2
λ (μm)	0.96	0.96
O.C.F (%)	7.53	7.85
N_v(cm^{-3})	1.429×10^{24}	1.429×10^{24}
N_{tr}(cm^{-3})	8.444×10^{23}	8.44×10^{23}
G_{th}(cm^{-1})	200.43	192
n_{th} (cm^{-3})	8.444×10^{23}	8.444×10^{23}

5.7 Conclusions

A detailed analysis of the tables shows that the band-offsets are greater in strain compensated structures compared to uncompensated structures. This is due to the fact that the band gap difference between tensile/compressive barrier and compressive/tensile strained quantum well is greater than conventionally strained quantum well structure leading an increase in the band-offsets. More specifically, the HH band shifts above the LH band in the compressively strained quantum well layer while reverse occurs in the tensile barrier thus also contributing to the increase in the HH band-offset.

We have calculated that strain compensated structures has higher gain compared to their corresponding uncompansated structures. Tan et. al. [7] have observed that their strain compensated structure's maximum gain is almost double that of the unstrained structure. There isn't such a large increase in gain calculations in our structures. Because we have tried to find similar, uncompensated structures to the compensated one, which have forced us to use different alloys in some cases. In our calculations most of the effect are coming from the band-offset differences.

CHAPTER 6

MODIFICATION OF VALANCE BAND STRUCTURE BY STRAIN COMPENSATION

6.1 Introduction

The combination of strain and quantum size effects has been used to modify the valence band structures for improving device characteristics. For example, introducing a biaxial compression in the quantum well plane reduces significantly the density of states in the valence band, leading to enhanced lasing properties [38, 39]. On the other hand, the introduction of biaxial tension increases the optical dipole for the lasing transition, resulting in an improved gain and reduced threshold current density [40, 41]. However, the tailoring of the valence band structure has mainly been determined in terms of the energy separation and mixing between heavy-and light-hole states [42].

The strain-compensated system is the one of the way to achieve to reduce the mixing between heavy- and light- hole states further by minimising the overlap between their envelope functions. This can be done by spatially separating them to different layers of superlattice stack. The compression and tension strains give also extra degrees of freedom to independently optimize the spatial overlap between heavy- and light-hole states as well as their zone-centre energy separation. Furthermore, strain-compensated strained-layer superlattices where opposite strains are introduced in the well and barrier regions offer significant advantages over uncompensated structures in which strain exists in the well material only [43].

In a strain system, as the quantum well thickness approaches some critical value, relaxation due to misfit dislocations occurs and eventually degrades the laser performance [44]. Also, as the number of strained wells is increased, the total strain accumulates and the critical thickness for the superlattice structure can be approached. In a strain-compensated system, the opposite strains balance each other and the average strain in a single period is reduced. The well width and total number of wells can thus be increased, leading to an enhanced optical confinement. A strain –compensated structure in which the light-hole and heavy-hole states are spatially separated with maximum zone-centre energy separation offers a significant improvement in the reduction of the threshold current density of quantum well lasers [45].

6.2 The Effect of Compression and Tension Strain on The Valance Band

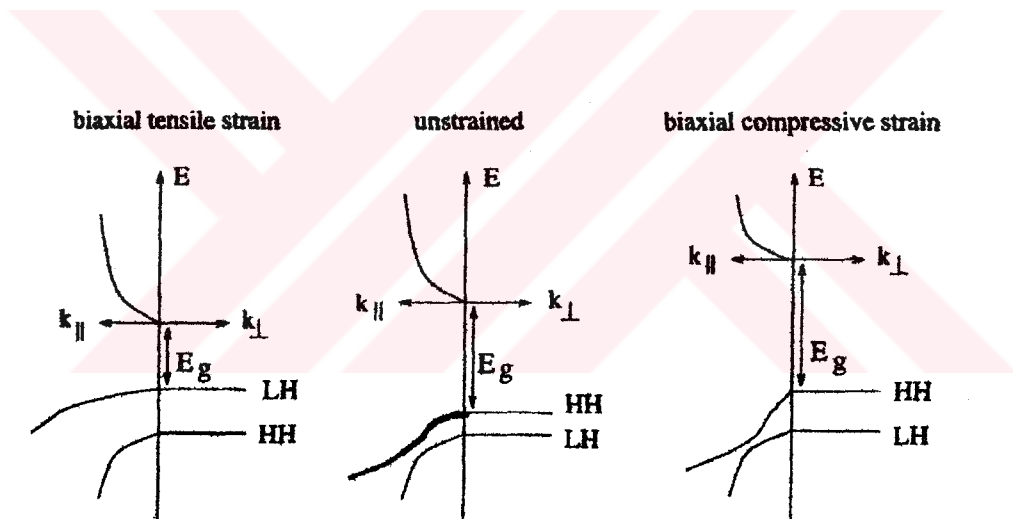biaxial tensile strain   unstrained   biaxial compressive strain

Fig.6.1   Schematic diagram of energy bands in a semiconductor quantum well near the Brillouin zone center; unstrained (center), under biaxial compressive strain (right), and under tensile strain (left). $k_\perp$ levels represents the growth direction wavevector, while the $k_\parallel$ represents the in-plane wavevector.

Axial strain splits the degeneracy of the light- and heavy-hole zone- centre states, accessing a wide range of subband structures, including the possibility of the highest valance subband being light-hole like, of significant benefit for semiconductor lasers. Since the strain can alter the heavy-hole, light-hole separation and hence the band occupation at threshold, it is possible to tailor the emission polarisation of the laser light.

The effect of compression and tension strain on the valance band of the quantum wells is shown in Fig.6.1. Fig.6.1 is a schematic diagram of the energy bands in semiconductor with combined quantum confinement and strain effects. The effect of quantum confinement on the ground state energy levels in a QW is a indicated by the horizontal lines in the direction perpendicular to the epitaxial layer. In the unstrained case (center of Fig.6.1), the quantum confinement effect alone results in the heavy-hole state being the highest valence band state and the energy difference between the light- hole and heavy –hole bands varies with the depth of the well and well width. The lowest energy transition which dominates the optical spectra of such structure is from conduction band to the highest valence band state. In addition to altering the bandgap energy and shapes of the valence bands, biaxial strain also lifts the light- and heavy-hole degeneracy at the zone center of the bulk semiconductors. Compressive strain increases the bandgap and puts the heavy-hole band above the light-hole band, which is similar to the effect of quantum confinement. Therefore, a combination of compressive strain and quantum effects maintains the position of the heavy-hole as the as the highest valence band state (right side of the Fig.6.1) with a reduced heavy-hole subband mass along $k_{||}$ direction. On the other hand, tensile strain decreases the bandgap and can lift the light-hole above the heavy-hole (left side of Fig.6.1) which is opposite to the quantum confinement effect. Then, the lowest energy optical transitions are between the conduction band and light-hole band. Under tensile strain, the mass along growth direction is reduced leading a large splitting between the light-hole subband in the quantum well structure. Thus a combination of the tensile-strain and quantum confinement results either the heavy-hole being the highest valance band state, degenerate light-hole and heavy-hole states, or the light –hole being the highest state, depending on the relative strengths of the two effects.

57

6.3 Bands Line-up (Type-I and Type-II)

An important feature of heterostructures is the way in which the conduction and valence band line up at the interface between the materials. This is particularly important for understanding in which material the electrons and holes will tend to be found (i.e., in which material they have the lower energy), and the extent to which they are confined in those materials. Fig.6.2 illustrates the terminology for the heterostructure interface.
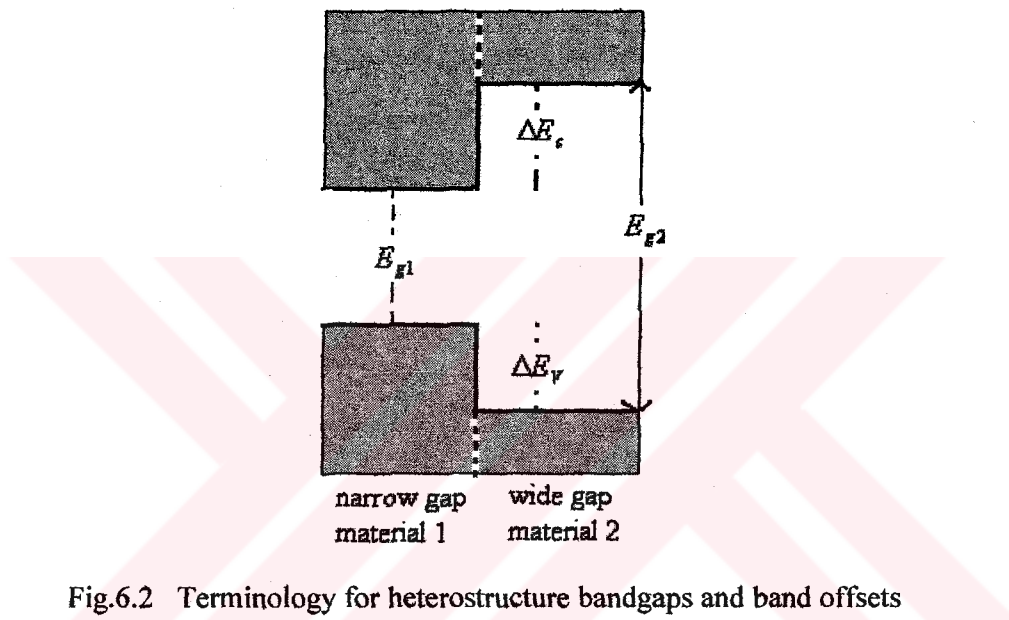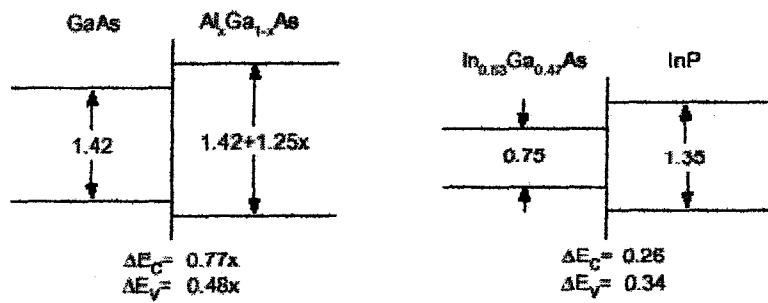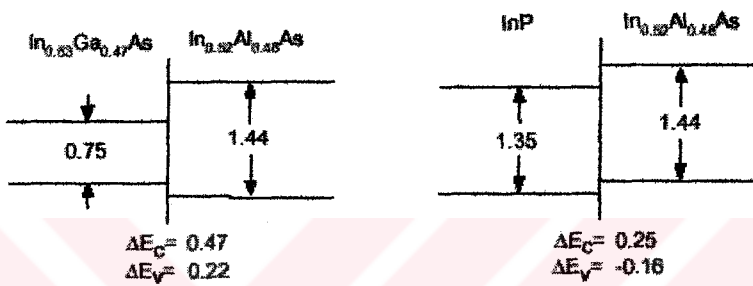

Fig.6.2   Terminology for heterostructure bandgaps and band offsets

In Fig.6.2, ΔE_c is called as the conduction band offset, and ΔE_v is called the valence band offset. Fig.6.3 shows typical values for the bandgaps and the offsets for various interfaces that are commonly used or investigated.
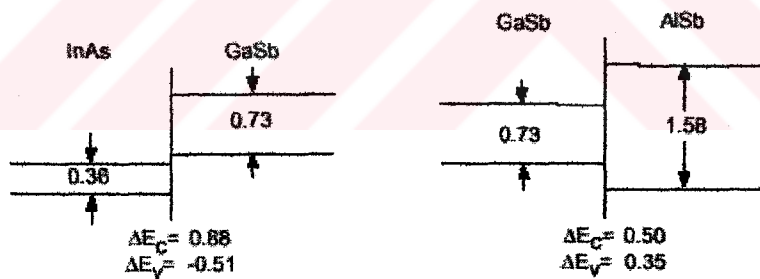
For optoelectronics, the most useful kind of band line-up is the kind shown in Fig.6.2, in which the electrons and the holes find lower energies in the narrower gap material ; this is known as a "Type I" band line-up. One reason why this line-up is important is that we usually want to have the electrons and holes in the same place so they can recombine efficiently in laser operation.

GaAs   Al$_x$Ga$_{1-x}$As

1.42   1.42+1.25x

ΔE_c= 0.77x
ΔE_v= 0.48x

In$_{0.53}$Ga$_{0.47}$As   InP

0.75   1.35

ΔE_c= 0.26
ΔE_v= 0.34

(a)

In$_{0.53}$Ga$_{0.47}$As   In$_{0.52}$Al$_{0.48}$As

0.75   1.44

ΔE_c= 0.47
ΔE_v= 0.22

InP   In$_{0.52}$Al$_{0.48}$As

1.35   1.44

ΔE_c= 0.25
ΔE_v= -0.16

(b)

InAs   GaSb

0.73

0.36

ΔE_c= 0.88
ΔE_v= -0.51

GaSb   AlSb

0.73   1.58

ΔE_c= 0.50
ΔE_v= 0.35

(c)

Fig.6.3   Band gaps and band offsets for various common III-V heterojunctions. All energies are in electron-volts (eV). (After Ref. [46], based on data collected in Ref. [47]).

Some important material combinations giving "Type 1" line-up include GaAs – Al$_x$Ga$_{1-x}$As, In$_{0.53}$Ga$_{0.47}$As - InP, and In$_{0.53}$Ga$_{0.47}$As - In$_{0.52}$Al$_{0.48}$As. Note that InP -

59

$In_{0.52}Al_{0.48}As$ is thought not to have this line-up, having instead lower electron energy in InP and lower hole energy in $In_{0.52}Al_{0.48}As$. Other extreme types of band line-up are also possible, as in the case of InAs - GaSb, in which the bottom of the conduction band of InAs is below the top of the valence band of GaSb; in this case a structure made of thin alternate layers of the two materials will have excess charge carriers in all layers without any doping since electrons from the GaSb valence band will "fall" into the InAs conduction band, and holes from the InAs conduction band will "fall" into the GaSb valence band, and the material is then known as a semimetal rather than a semiconductor.

6.4 Light-hole Spatial Separation

A Ghiti et al.[45] considered the possibility of spatially separating the light-hole states from the electron and heavy-hole states.
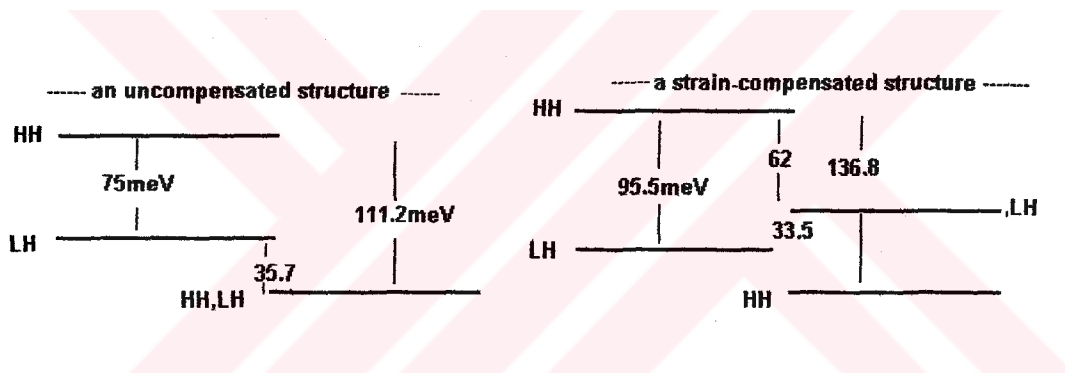

Fig.6.4   Valance band line-ups for an uncompensated $In_{0.97}Ga_{0.03}As_{0.51}P_{0.49}/$ $In_{0.78}Ga_{0.22}As_{0.48}P_{0.52}$ structure and a strain- compensated $In_{0.89}Ga_{0.11}As_{0.78}P_{0.22}/$ $In_{0.43}Ga_{0.57}As_{0.92}P_{0.08}$ structure. InP is the substrate material in both cases.

Fig.6.4 shows the valance band line-ups for an uncompensated structure consisting of $In_{0.97}Ga_{0.03}As_{0.51}P_{0.49}$ wells under 1.4% compression and $In_{0.78}Ga_{0.22}As_{0.48}P_{0.52}$ lattice-matched barriers, and a strain- compensated structure consisting of $In_{0.89}Ga_{0.11}As_{0.78}P_{0.22}$ wells under 1.7% compression and $In_{0.43}Ga_{0.57}As_{0.92}P_{0.08}$ barriers under 1% tensile strain. These structures are selected in order to show clearly the effects on the dispersion of spatially seperating the heavy- and light- hole states. The uncompensated structure offers a Type-I line-up for both

heavy- and light-hole states whereas in the compensated structure, the light-holes have a Type II line-up.

The calculated valance subband dispersions for the compensated and uncompensated structures are shown in Fig.6.5 by including the heavy-hole, light-hole, spin-orbit and electron states structure in the $k.p$ Hamiltonian [48] and using the finite difference method [49,50]. Author concentrate on the dispersion of the highest hole subband because most injected holes populate it.

Fig.6.5 Valence subband structure for the uncompensated (full curves) and strain-compensated (broken curves) structures.

Fig.6.5 shows that although the H_1-L_1 zone-centre energy separation is smaller in the compensated structure, H_1 has a light-hole cap (a subband dispersion corresponding to a small parallel mass) which extends over a wider energy range. This is due to the reduction of the spatial overlap between H_1 and the light hole state, especially L_1

61

6.5 Heavy-hole Spatial Separation

In this section, we consider separating the heavy-hole states from the light-hole and electron states. This could be of great benefit for strained-layer lasers whose active material is under biaxial tension because these have improved gain and differential gain over compressive lasers [51,52]. Following the same procedure outlined above , author found that AlGaAsSb wells under tension and AlGaAsSb barriers under compression grown on GaSb offer this possibility. However, the maximum compressive strain that can be obtained is 0.65%, i.e that of AlSb on GaSb using the parameters from [6].
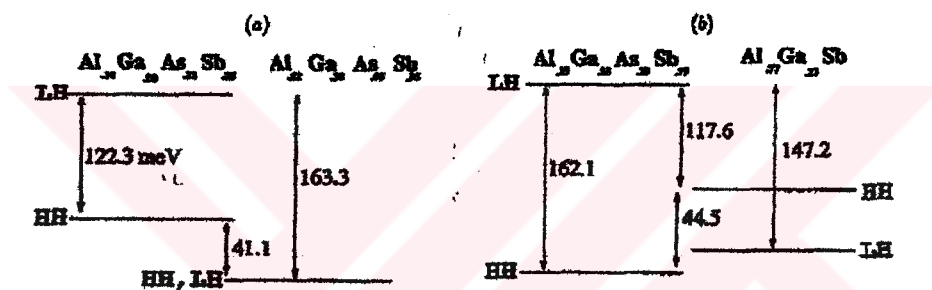
Fig.6.6   Valence band line-up for (a) an uncompensated $Al_{0.1}Ga_{0.9}As_{0.22}Sb_{0.78}$ / $Al_{0.62}Ga_{0.38}As_{0.05}Sb_{0.95}$ structure and (b) a strain-compensated $Al_{0.15}Ga_{0.85}As_{0.29}Sb_{0.71}$/ $Al_{0.77}Ga_{0.23}Sb$ structure. GaSb is the substrate material in both cases.

A strain-compensated structure, consisting of $Al_{0.15}Ga_{0.85}As_{0.29}Sb_{0.7}$ wells under 2% tensile strain and $Al_{0.77}Ga_{0.23}Sb$ barriers under 0.5% compressive strain, and a comparison with an uncompensated structure, consisting of $Al_{0.1}Ga_{0.9}As_{0.22}Sb_{0.78}$ wells under 1.6% tension and $Al_{0.62}Ga_{0.38}As_{0.05}Sb_{0.95}$ lattice matched barriers. The valence band line-ups for the two structures are shown in Fig.6.6. They have opposite heavy-hole offsets, with the heavy-hole states having a type-II line-up in the compensated structure. The strain in the compensated well is higher than in the uncompensated well in order to have equal energy separation between the first light- and heavy-hole states.
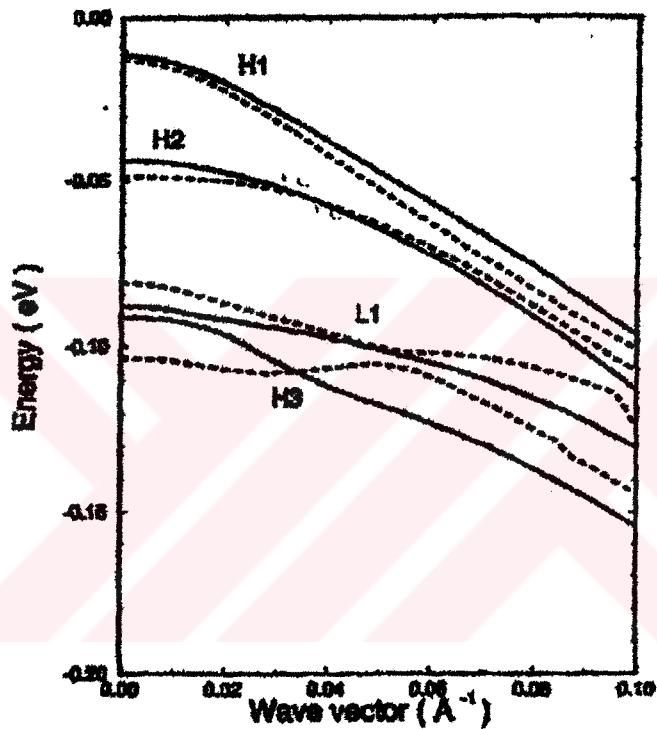
62
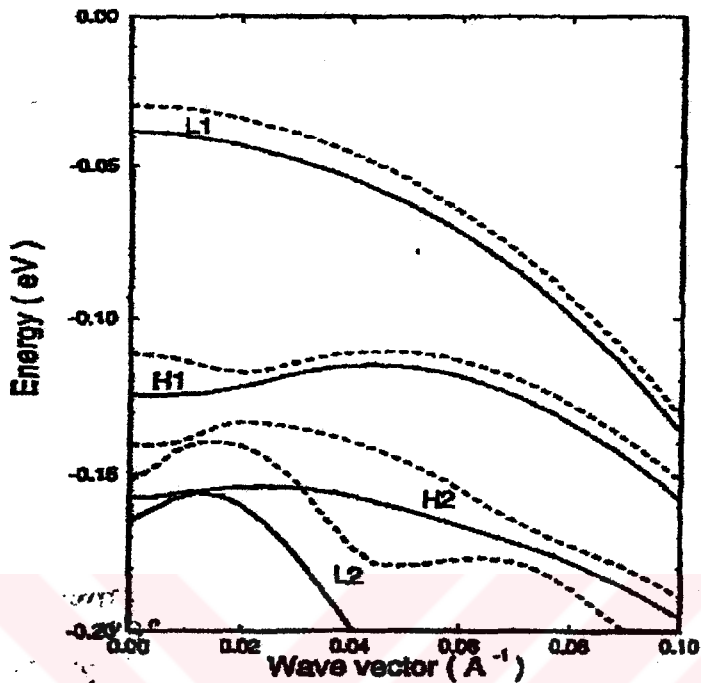
Fig.6.7 Valence subband structure for the uncompensated (full curves) and strain-compensated (broken curves) structures.

The valance band structures are shown in figure 6.7, taking 70Å well-width and 80Å barrier-width respectively. Despite the reduction of the L_1-H_1 energy separation, the compensated structure has a slightly steeper dispersion. This again clearly shows the importance of the spatial overlaps between the highest light-hole and the other heavy-hole states.

6.6 The Band Line-up Investigation of the QT(cs) and QT(ts) structures

In the following subsections we determine the type of the band line-ups in our laser structures and compare it with their conventional correspondings.

6.6.1 QT(cs) structure at 1.27μm

a-)Compensated   b-) uncompensated

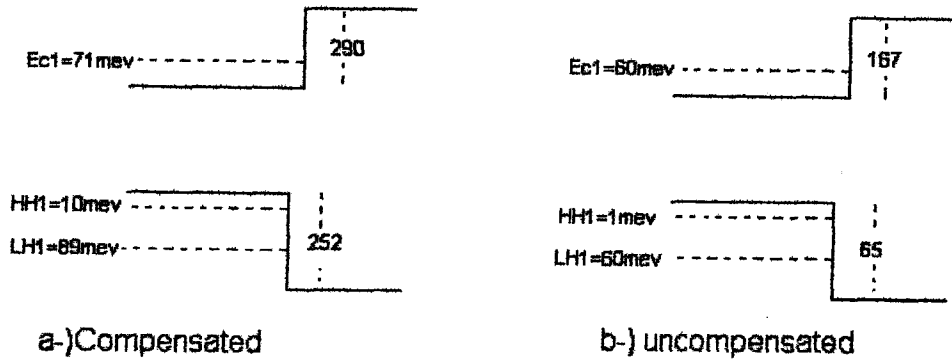Fig.6.8   Valence band line-up (a) QT(cs) compensated and (b) QT(cs) uncompensated structures

Fig.6.8 shows the valence band line-up for (a) $In_{0.89}Ga_{0.11}As_{0.56}P_{0.44}/In_{0.92}Ga_{0.08}P$-InP QT(cs) strain compensated and (b) $In_{0.89}Ga_{0.11}As_{0.56}P_{0.44}/$ $In_{0.746}Ga_{0.254}As_{0.55}P_{0.45}$ -InP QT(ts) uncompensated structures. The separation between heavy-hole and light-hole is bigger in compensated structure compared to that of the uncompensated structure. These two structures obey Type-I and transition happens between Ec1 and HH1.

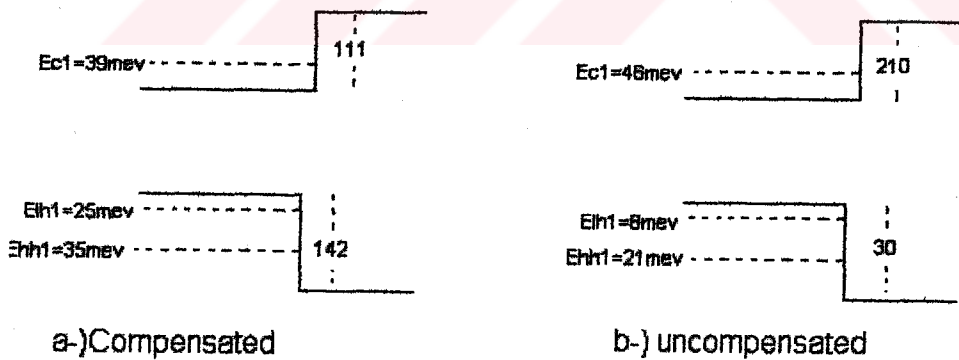### 6.6.2 QT(ts) structure at 1.33μm

a-)Compensated   b-) uncompensated

Fig.6.9   Valence band line-up (a) QT(ts) compensated and (b) QT(ts) uncompensated structures

Fig.6.9 shows the valence band line-up for (a) $In_{0.55}Ga_{0.45}As_{0.81}P_{0.19}/In_{0.24}As_{0.76}P$-InP QT(cs) strain compensated and (b) $In_{0.55}Ga_{0.45}As_{0.76}P_{0.24}/$ $In_{0.746}Ga_{0.254}As_{0.55}P_{0.45}$ -InP

QT(ts) uncompensated structures. The separation between heavy-hole and light-hole is bigger in compensated structure when it is compared with uncompensated structure. This two structure obey the type-I and transition happens between Ec1 and LH1.

6.7 Results and Discussions

The analysis of the structures emitting at 1.27μm and 1.33μm shows that all structures have type-I band line-up. Therefore, in these structures the minimum energy of both HH and LH lies in the same layer. This results a higher density of states and higher threshold characteristics. So if one could separate one of the valence band into the next lying layer, i.e. into the barrier, the density of states will be reduced resulting low threshold characteristics. In spite of this, we should take into account the fact that the energy level separations are enhanced in strain-compensated structures. This reduce the extent of mixing and coupling between the subbands, therefore, reducing the threshold characteristics.

As an overall, the spatial separation of valence bands will certainly bring extra benefits to the strain-compensated lasers, in device designing.

CHAPTER 7

CONCLUSIONS

The work carried out in this thesis considered the effect of compensating a strained active layer on optical confinement factor, conduction- and valence-band offsets, allowed energy levels, transparency and threshold carrier density, peak gain and band line-ups. In each of the results chapter appropriate conclusions have already been presented. However, it is useful in this chapter to gather together the major conclusions from the work described in this thesis.

It is seen from this work that strain-compensated structures can be obtained by using appropriately opposite strained barriers to that of the active layer so that the net strain of the multi-quantum well region is approximately zero. Strain compensation technique allows one to determine the limits of maximum strain that can be incorporated into quantum wells and be strain-compensated to achieve a zero net-strain system. In lasers that require high gain and thus many quantum wells strain compensation may be used to increase the number of compressively strained wells without inducing defects.

Strain compensation also gives access to a wider range of material compositions, and thus improved possibilities to select band-edge offsets tailored to specific device needs. Therefore, growth parameters can be optimized by means of strain compensation which allows large number of wells to be grown. We present band-offset ratios for our strain-compensated laser structures using Model Solid Theory and Harrison Model. The trend that we have obtained using Harrison model is in agreement with experimental values. The comparison of valence and conduction band-offset's for the two laser structures reveals the fact that the wells are deeper in

66

the case of compressively strained active layers than that of tensiley strained active layers in strain-compensated structures.

Calculated results using the examples of strain-compensated and a comparable strained quantum well lasers indicate that the strain-compensation improves the optical confinement factor and modifies the band structure. These modifications result reduced transparency and threshold characteristics which is a great benefit in lasers. Our results indicate that strain compensated structures with compression wells are suitable for device applications when a large number of quantum wells is required. Furthermore, modification of the strain compensated quantum well band structure may result in novel low dimensional physical properties.

REFERENCES

[1]   J. W. Matthews and A. E. Blakeslee, J. Cryst. Growth **24** (1974) 188.

[2]   T. L. Koch, U. Koren, R. P. Gnall, C. A. Burrus, and B. I. Miller, Electron. Lett. **26** (1988) 1431.

[3]   E. Yablonovitch and E. O. Kane, J. Lightwave Technol. **6** (1988) 1292.

[4]   N. K. Dutta, W. S. Hobson, D. Vakhshoori, H. Han, P. N. Freeman, J. F. de Jong, and J. Lopata, IEEE Photon. Technol. Lett. **8** (1996) 852.

[5]   T.C. Chong and C.G. Fonstad , IEEE J. Quantum Electron. **QE-25** (1989) 171.

[6]   M.P. Krijn, Semiconductor. Sci. Technol. **6** (1991) 27.

[7]   G. L Tan and J. M. Xu,, IEEE Photonic Technology letters **10** (1998) 1386.

[8]   C.G. Van de Walle, Phys. Rev.B **40** (1989) 1871.

[9]   Z.M. Li, M. Dion, Y. Zou, J. Wang, M. Davies, and S.P. McAlister, IEEE J. Quantum Electron. **QE-30** (1994) 538.

[10]   W.W. Chow, S. W. Koch, and M. Sargent,(*Semiconductor-Laser Physics* 1994).

[11]   H. Haug and S.W. Koch, Phys. Rev. A, (1989) 1887.

[12]   D. Ahn and L. Chuang, IEEE J. Quantum Electron. **QE-30** (1994) 350.

[13]   N.K Dutta, J. D. Wynn, D. L. Sivco, and A. Y. Cho, Appl. Phys. Lett. **56** (1990) 2293.

[14]   G.P.Agrawal and N.K.Dutta, *(Semiconductor lasers.* New York: van Nostrand Reinhold Co. 1992).

[15]   Seoung-Hwan Park, Byung- Doo Choe, Weong-Guk Jeong, Appl. Phys. Lett. **66** (1995).

[16]   J. Christopher Dries, Milind R. Gokhale, Hiroyuki Uenohara, and Stephen R. Forrest., IEEE Photonic Technology letters **10** (1998).

[17]   B. GONUL, *(A Theoretical study of the threshold current of quantum well lasers Ph. D. Thesis* 1995).

[18]   J. Vurgaftman et al., J. Appl. Phys. **89** (2001) 11.

[19]   J. Minch, S. H. Park, T. Keating, and S. L. Chuang, IEEE Journal of Quantum Electronics **35** (1999) 5.

[20]   S. H. Groves, J. N. Walpole, L. J. Missaggis, Appl. Phys. Lett. **61** (1992) 255.

[21]   A. Ponchet, A. Rocher, A. Ougazzaden, A. Mircea, J. Appl. Phys. **75** (1994) 7881.

[22]   P. J. A. Thijs,T. Van Dongen, Electron. Lett. **25** (1989) 1735.

[23]   A. Bhattacharya, D. Botez, Appl. Phys. Lett. **72** (1998) 138.

[24]   G. Zhang, A. Ovtchinnikov, Appl. Phys. Lett. **62** (1993) 1644.

[25]   A. Ougazzaden, F. Devaux, E. V. K. Rao, L.Silvestre, G. Patriarche, Appl. Phys. Lett. **70** (1997) 96.

[26]   H. C. Kuo, S. Thomas, T. U. Horton, B. G. Moser, G. E. Stillman, C. H. Lin, H. Chen, J. Vac. Sci. Technnol.B **36** (1998) 1377.

[27]   M. Toivonen, P. Savolainen, H. Asonen, R. Murison, J. Vac. Sci. Technol. B **30** (1996) 1736.

[28]   C. Silfvenius, B. Stalnacke, G. Landgren, Journal of Crystal Growth **170** (1997) 122.

[29]   S. L. Chuang, (*Physics of Optoelectronic Devices. Newyork: Wiley* 1995).

[30]   C. G. Van de Walle, Phys. Rev. B **39** (1989) 1871.

[31]   W. A. Harrison, J. Vac. Sci. Technol. **14** (1977) 1016.

[32]   M. Yamamoto, N. Yamamoto and J. Nakano, in: 5th Int.Conf. on InP and Related Materials, Paris, France, (1993) 231.

[33]   K. Mori, M. Takemi, T. Takiguchi, K. Goto, T. Nishimura, T. Kimura, Y. Mihashi and T. Murotani, in: 5th Int.Conf. on InP and Related Materials, Paris, France (1993) 235.

[34]   P. J. A. Thijs, T. V. Dongen, L. F. Tiemeijer and J. J. M. Binsma, J. Lightwave Technol. **12** (1994) 28.

[35]   A. Ponchet, A. Rocher, A. Ougazzaden, A. Mircea, A. G. Cullis and A. E. Staton- Bevan, in: Proc. to Microscopy of Semiconducting Materials, Oxford, UK (1995) 199.

[36]   N. Yokouchi, N. Yamanaka, N. Iwai, T. Matsuda and A. Kasukawa, in: 7th Int.Conf. on InP and Related Materials, Hokkaido, Japan (1995) 57.

[37]   K. J. Vahala and C. E. Zah, Appl. Phys. Lett. **52** (1998) 1945.

[38]   A. R. Adams, Electron. Letter **22** (1986) 249.

[39]   E. Yablonovitch and E. O. Kane, IEEE J. Lightwave Tech. **4** (1986) 961.

[40]   C. E. Zah., R. Bhat, B. Pathak, C. Caneau, F. J. Favire, N. C. Andreakis, Electron Lett. **27** (1991) 1414.

[41]   P. J. A. Thijs, J. J. M Binsma, L. F Tiemeijer and T. Van Dongen, Proc. European Conf. on Optical Communication (1991) 31.

[42]   E. P. O'Reilly, Semicond. Sci. Technol. **4** (1989) 121.

[43]   B. I. Miller, U. Koren , M. G. Young and M. D. Chien, Appl. Phys. Lett. **58** (1991) 1952.

[44]   P. Voison ,(*Proc. SPIE: Proceedings, Quantum Wells and Superlattices in Optoelectronic Devices and Integrated Optics* 861, (1987) 88).

[45]   A. Ghiti and U. Ekenberg, Semicond. Sci. Technol **9** (1994) 1575.

[46]   W. R. Frensley, (*Heterostructure and Quantum Well Physics in Heterostructures and Quantum Devices* 1994).

[47]   E. T. Yu, J. O. McCaldin, and T. C. McGill, Solid State Physics Advanced in Research and Applications **46** (1992) 2.

[48]   A. M . Cohen. and G. E. Marques , Phys. Rev. B **41** (1990) 10608.

[49]   B. Jogai and P. W. Yu , Phys. Rev. B **41** (1990) 12650.

[50]   C . Juang, K. J. Kuhn, and R. B. Darling, Phys. Rev. B **41** (1990) 12047.

[51]   A. Ghiti, M. Silver and E. P. O'Reilly, J. Appl. Phys. **71** (1992) 4626.

[52]   P. J. A. Thijs, J. J. M. Binsma, L. F Tiemejer. And T. Van Dongen,
        Electron. Lett. **28** (1992) 829.

[53]   Paul Harrison, (*Quantum Wells, Wires and Dots, John Wiley & Sons Ltd.,*
        2000).

APPENDIX A

*The proof of the $x_b = \dfrac{(a_s - 5.4512 - \varepsilon_b * 5.4512)}{0.4176 * (\varepsilon_b + 1)}$ *****

Structure: $In_{1-x}Ga_xAs_yP_{1-y}$ /$In_{xb}Ga_{1-xb}P$/InP

We can obtain this relationship from the zero-net theory of

$$N_w t_w \varepsilon_w + N_b t_b \varepsilon_b \cong 0 \qquad\qquad (A.1)$$

where N_w is the number of the well, N_b is the number of the barrier, t_w and t_b are the the thicknesses of well and barrier, ε_w and ε_b are the strain of the well and barrier, correspondingly.

In Eqn.(A.1) a_s and a_{ew} are known , so the magnitude of the strain in the well

$$\varepsilon_w = \left(\frac{a_s}{a_{ew}}\right) - 1 \qquad\qquad (A.2)$$

where a_{ew} is the lattice constant of the well, a_s is the lattice constant of the substrate (a_{InP}=5.8688). The magnitude of the strain in the barrier

$$\varepsilon_b = \left(\frac{a_s}{a_{eb}}\right) - 1 \qquad\qquad (A.3)$$

where a_{eb} is the lattice constant of the barrier.
ε_b can be found from equation (A.1) as

73

$$\varepsilon_b = -\frac{N_w * _w * \varepsilon_w}{N_b * t_b} \qquad \text{(A.4)}$$

Let's equate equation (A.3) and (A.4)

where $a_{eb} = x_b * 5.8688 + (1 - x_b) * 5.4512$ from linear interpolation

$$\varepsilon_b = \left(\frac{a_s}{x_b * 5.8688 + (1 - x_b) * 5.4512} \right) - 1 \qquad \text{(A.5)}$$

$$\varepsilon_b * x_b * 5.8688 + \varepsilon_b * 5.4512 - \varepsilon_b * x_b * 5.4512 = a_s - 5.4512 - 0.4176 * x_b \qquad \text{(A.6)}$$

Rewritting equation (A.6)

$$x_b = \frac{(a_s - 5.4512 - \varepsilon_b * 5.4512)}{0.4176 * (\varepsilon_b + 1)} \qquad \text{(A.7)}$$

74

APPENDIX B

*The proof of the $x_b = \dfrac{(a_s - 5.8688 - \varepsilon_b * 5.8688)}{0.1896 * (\varepsilon_b + 1)}$ *****

Structure: $In_{1-x}Ga_xAs_yP_{1-y}$ /$In_{xb}As_{1-xb}P$/InP

We can obtain this relationship from the zero-net theory of

$$N_w t_w \varepsilon_w + N_b t_b \varepsilon_b \cong 0 \tag{B.1}$$

where N_w is the number of the well, N_b is the number of the barrier, t_w and t_b are the the thicknesses of well and barrier, ε_w and ε_b are the strain of the well and barrier, correspondingly.

In Eqn.(B.1) a_s and a_{ew} are known , so the magnitude of the strain in the well

$$\varepsilon_w = \left(\frac{a_s}{a_{ew}} \right) - 1 \tag{B.2}$$

where a_{ew} is the lattice constant of the well, a_s is the lattice constant of the substrate (a_{InP}=5.8688). The magnitude of the strain in the barrier

$$\varepsilon_b = \left(\frac{a_s}{a_{eb}} \right) - 1 \tag{B.3}$$

where a_{eb} is the lattice constant of the barrier.

ε_b can be found from equation (B.1) and given in equation (B.4)

$$\varepsilon_b = -\frac{N_w * \varepsilon_w}{N_b * t_b} \qquad \text{(B.4)}$$

Let's equate equation (B.3) and (B.4)

where $a_{eb} = x_b * 6.0584 + (1 - x_b) * 5.8688$ from linear interpolation

$$\varepsilon_b = \left(\frac{a_s}{x_b * 6.0584 + (1 - x_b) * 5.8688} \right) - 1 \qquad \text{(B.5)}$$

$$\varepsilon_b * x_b * 6.0584 + \varepsilon_b * 5.8688 - \varepsilon_b * x_b * 5.8688 = a_s - 5.8688 - 0.1896 * x_b \qquad \text{(B.6)}$$

Rewritting equation (B.6)

$$x_b = \frac{(a_s - 5.8688 - \varepsilon_b * 5.8688)}{0.1896 * (\varepsilon_b + 1)} \qquad \text{(B.7)}$$

76

APPENDIX C

Allowed energy levels are calculated using the following Eqn's of

$$\tan\left(k_z \frac{l_z}{2}\right) = \frac{m_w}{m_b}\left(\frac{\alpha_z}{k_z}\right) \quad \text{(even)} \qquad \text{(C.1)}$$

$$\cot\left(k_z \frac{l_z}{2}\right) = -\frac{m_w}{m_b}\left(\frac{\alpha_z}{k_z}\right) \quad \text{(odd)} \qquad \text{(C.2)}$$

Equation (C.1) and (C.2) are even and odd solutions of the Schröndinger's equation for a finite well at interface [53]. l_z is width of the quantum well width and

$$k_z^2 = \frac{2m_w}{\hbar^2} E_c \qquad \text{(C.3)}$$

$$\alpha_z^2 = \frac{2m_b}{\hbar^2}[V_0 - E_c] \qquad \text{(C.4)}$$

Even and odd solutions are calculated numerically in terms of the following way. Say the left side of Eqn. (C.1) is w and the right of Eqn. (C.1) is q:

$$w = \tan\left(k_z \frac{l_z}{2}\right), \text{ and} \qquad \text{(C.5)}$$

$$q = \frac{m_w}{m_b}\left(\frac{\alpha_z}{k_z}\right) \qquad \text{(C.6)}$$

w is an increasing function, q is a decreasing function . We observe true allowed energy levels at intersection of w and q. But ,we can not observe all . So, the intersection of w and q gives the allowed energy levels in terms of the given parameters of m_w, m_b, V_0 and l_z. This is illustrated in Fig.C.1
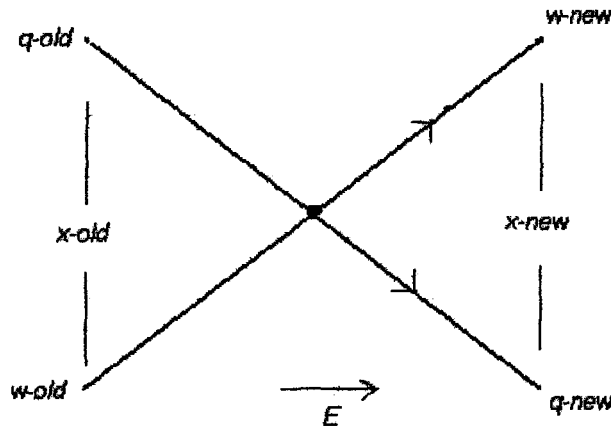

Fig.C.1 Schematic diagram of w and q function

Since w and q varies linearly (y=ax+b), they can be written in the following form of

$$w(E) = w_{old} + (E - E_{old})\frac{(w_{new} - w_{old})}{\Delta E}, \text{ and} \qquad (C.7)$$

$$q(E) = q_{old} + (E - E_{old})\frac{(q_{new} - q_{old})}{\Delta E} \qquad (C.8)$$

$$\text{where } \Delta E = E_{new} - E_{old} \qquad (C.9)$$

Equating Eqn.(C.7) and (C.8), we obtain

$$w_{old} + (E - E_{old})\frac{(w_{new} - w_{old})}{\Delta E} = q_{old} + (E - E_{old})\frac{(q_{new} - q_{old})}{\Delta E} \qquad (C.10)$$

78

Rearranging equation (C.10)

$$x_{old} = q_{old} - w_{old} = (E - E_{old})\left[\frac{x_{old} - x_{new}}{\Delta E}\right]$$

(C.11)

Rearranging equation (C.11)

$$E = E_{old} + \left(\frac{x_{old}.\Delta E}{x_{old} - x_{new}}\right)$$

(C.12)

In the same way

$$E = E_{new} - \left(\frac{x_{new}.\Delta E}{x_{old} - x_{new}}\right)$$

(C.13)